NASA TECHNICAL MEMORANDUM 107742

MONITORING DAMAGE GROWTH IN TITANIUM MATRIX COMPOSITES USING ACOUSTIC EMISSION

J. G. Bakuckas, Jr., W. H. Prosser, and W. S. Johnson

March 1993

National Aeronautics and Space Administration

Langley Research Center
Hampton, Virginia 23681-0001

Abstract

In this study, the application of the acoustic emission (AE) technique to locate and monitor damage growth in titanium matrix composites (TMC) was investigated. Damage growth was studied using several optical techniques including a long focal length, high magnification microscope system with image acquisition capabilities. Fracture surface examinations were conducted using a scanning electron microscope (SEM). The AE technique was used to locate damage based on the arrival times of AE events between two sensors. Using model specimens exhibiting a dominant failure mechanism, correlations were established between the observed damage growth mechanisms and the AE results in terms of the events amplitude. These correlations were used to monitor the damage growth process in laminates exhibiting multiple modes of damage. Results from this study revealed that the AE technique is a viable and effective tool to monitor damage growth in TMC.

Introduction

The acoustic emission (AE) technique is a nondestructive evaluation (NDE) method which uses stress waves emitted by stressed material undergoing deformation processes such as plastic deformation or crack growth. There are two main differences between the AE technique and other NDE methods [1]: (1) the signal is generated internally by the material and not by an external source, and (2) internal movements are detected using the AE technique while internal structures are detected using other NDE methods. One advantage of the AE technique is that it can be used efficiently on a large structure to locate non-visual damage in real-time (during service conditions). Once the damage site is located, other NDE methods can be used to further assess the criticality of the defect.

As a stress wave or AE signal travels through a material, its characteristics are constantly changing due to attenuation, damping, boundary surface interactions, etc. These signal changes are called propagation alterations. In addition, detection alterations occur to the stress wave due to the AE hardware receiving the signal (sensors, cables, amplifiers, etc.). Consequently, a stress wave recorded by the AE equipment is a transformed representation of the original source wave.

In general, there are two major branches of AE research. The first branch is called the quantitative AE approach or Source Function Analysis (SFA) which are methods to characterize the source AE signals [1-3]. High fidelity (broadband) sensors are used to obtain information about the waveform of the source AE signal over a wide range of frequencies. The propagation and detection alterations of the source AE signal are modeled using transfer functions. With these transfer functions, a source function is determined by a deconvolution process. The resulting source function provides a full description of the source AE signal independent of the material properties, the specimen geometry, and the AE hardware. In theory, the damage modes observed in a small specimen can be correlated to the source AE signal. This correlation can then be directly applied to a large structure to identify the damage modes. However, the SFA approach has limited application due to the complex analysis and the extensive computing capacity required to analyze a single event. Currently, the SFA methods are not practical for composite materials where numerous AE signals are generated and the inhomogeneous, anisotropic nature of the composite further complicates the analysis.

The second major branch of AE research is called the conventional AE technique. In this approach, highly resonant sensors are used; these sensors are more sensitive than broadband sensors but further alter the signal. In this technique, certain features or parameters of the AE waveform which can be efficiently and quickly processed are analyzed. A typical AE waveform with these signal features is shown schematically in Figure 1. Since the propagation and detection alterations on the signal are not considered, these AE parameters are strongly dependent on the geometry and material properties of the specimen as well as the sensor and detection electronics. The application of conventional AE technique has had success when a large number of similar specimens are tested. For example, the conventional AE techniques have been extensively used to determine the structural integrity of utility bucket trucks and chemical storage tanks [4-7]. In the remaining text, only the conventional AE techniques will be used and will be referred to simply as AE techniques.

The use of the AE technique to monitor damage growth in composite materials during small scale laboratory testing has been studied extensively [7-14]. As shown in these studies, the AE technique offers a very effective method capable of locating and detecting non-visual damage and tracking its progression and accumulation in real-time. A detailed analysis of the AE event parameters could identify the actual type of damage. Correlations between the AE parameters, particularity the event amplitude, and source damage modes have been established in a number of investigations. However, these correlations are not universal due to the dependency of the AE parameters on the specimen geometry, material properties and AE hardware.

It should be pointed out that the interpretation of AE data to monitor damage growth in composite materials is a difficult task. Damage growth is a complex process that must first be understood in order to apply the AE technique. An additional difficulty in the interpretation of AE data is friction [14]. Fracture surfaces are continuously being created as damage progresses. When fracture surfaces come in contact, they produce friction which results in AE events. These friction-generated emissions commonly occur during fatigue loading. The amount of friction-generated emissions will increase substantially as the rate of loading increases. Consequently, multiple AE events will be superimposed and will be erroneously recorded as a single event with increased values of the AE parameters. Care must be taken to insure that the friction-generated emissions are discriminated from the damage-generated emissions.

The objective of this study was to use the AE technique to monitor damage growth in an advanced titanium matrix composite (TMC) system. For comparison, damage growth was also monitored using several optical techniques including a long focal length, high magnification microscope system with image acquisition capabilities, a high magnification closed circuit television (CCTV) system, and an optical microscope. Examinations of fracture surfaces and of surface and edge replicas were conducted using a scanning electron microscope (SEM). The primary emphasis was placed on using the AE technique to locate damage, to establish a correlation between the AE results and the dominant failure mechanisms, and to monitor the damage growth process. A correlation was established between the damage growth mechanisms

and the AE events amplitude using model specimens which exhibited a dominant failure mechanism. This correlation was then used to identify and monitor damage in laminates exhibiting multiple modes of damage. It should be pointed out that only qualitative analyses of trends in the AE results were conducted in this research. No attempt was made to quantify the AE results.

Materials and Experimental Procedure

Materials and Specimens

The material tested in this study is an advanced titanium matrix composite designated SCS-6/β21S. The composition of the β21S titanium alloy is Ti-15Mo-3Al-2.7Nb-0.2Si. The composite laminates were fabricated by Textron by hot isostatic pressing (HIPing) β21S foils between unidirectional tapes of silicon-carbide (SCS-6) fibers having a diameter of 0.14 mm. The lay-ups studied were $[90]_4$, $[0]_4$, $[0/90]_s$, and $[0/90]_{2s}$ with a range of fiber volume fractions v_f of 0.34 to 0.38. In addition, fiberless neat β21S was fabricated according to the same process as that used for the composites.

Specimens with a length of 152.4 mm were cut using a diamond wheel saw into straight-sided coupons with the 0° fibers in the loading direction. Unnotched specimens with a width of 12.7-mm were tested to obtain the elastic properties and unnotched strengths. Both center hole and center notched specimens with widths W = 19.05-mm and W = 25.40-mm, respectively, were studied. The center hole specimens having a hole diameter to width ratio, d/W = 0.33, were machined using an ultrasonic drilling technique. The center notch specimens having notch length to width ratios, 2a/W, ranging from 0.2 to 0.5, were machined using wire electro-discharge machining (EDM). All specimens were heat treated at a temperature of 620°C for 8 hours prior to testing. To make optical observations and replicas, the surface of each specimen was polished to obtain a flat and lustrous finish. Aluminum end tabs were bonded on all specimens in order to prevent grip failure of the specimen and to minimize unwanted acoustic emissions in the gripped region.

Test Procedure

Static and fatigue tests were performed using a closed-loop servo-hydraulic test machine equipped with hydraulic grips. The static tests were conducted under stroke control at a rate of 0.05 mm/s. During static loading, each specimen was instrumented with an extensometer with a gage length of 25.4-mm to obtain global stress-strain and load-displacement curves for unnotched and notched specimens, respectively. For the unnotched specimens, the extensometer was placed on the edge of the specimens, and for the notched specimens, the extensometer was placed on the surface of the specimens with the notch in the center of the extensometer gage length. Fatigue tests were conducted under load control with an R-ratio (S_{min}/S_{max}) of 0.1 and a frequency of 3 Hz.

Damage initiation and growth was monitored and recorded using acoustic emission, a long focal length optical microscopic system with image acquisition capabilities, a high magnification (X150) closed circuit television (CCTV) system, scanning electron microscopy (SEM), and replicates. In two specimens, the matrix material was removed through an acid etching procedure to reveal fiber breaks. In addition, the residual strength of a specimen subjected to a prior fatigue loading history was measured under static loading.

Acoustic Emission Set-Up and Location Detection Algorithm

The AE testing equipment and test parameters were as follows: AE Data Acquisition System, Physical Acoustic Corp. (PAC) Model Locan AT; 150 kHz resonant sensors, PAC Model 15R; 40 dB preamplifiers having a 100 kHz - 300 kHz bandpass filter, PAC Model 1220A; 20 dB postamplifier gain; system threshold of 0.1, and; dead time of 1ms (used to distinguish between discrete events). Two sensors were attached to the specimen using elastic electrical tape. Each sensor was placed at equal distances approximately, ℓ = 30 mm, from the center-line of the notches as shown in Figure 2. Vacuum grease was used as a couplant between the sensors and the specimen surface.

A Hsu pencil lead break procedure (ASTM E976) was used for AE location calibration as described below. A mechanical pencil with 0.5 mm diameter 2H lead was used. The lead was broken on the edge of the specimen beside sensor 1 as shown in Figure 2, and the arrival time of

the signal at sensor 1, t_1^{cal}, and at sensor 2, t_2^{cal}, was measured. The difference in these arrival times ($\Delta t_{gage} = t_2^{cal} - t_1^{cal}$) is the time it took the AE signal to propagate from sensor 1 to sensor 2. The same procedure was repeated for sensor 2. The Δt_{gage} measured beside each sensor was compared to insure that they were similar. An average Δt_{gage} was calculated from several lead breaks. Care was taken to break the lead at the same length and at the same angle with respect to the specimens edge. This insured reproducible impulse type signals which were easily recorded by the AE system. As a final check, a lead break was made at the center of the sensor gage length (i.e. at the notch) to insure ($t_2 - t_1$) was close to zero. Knowing Δt_{gage}, the distance between the AE sensors, ℓ, and the arrival times of an AE event at both sensors, t_1 and t_2, the location of an AE event, X, was determined from linear interpolation:

$$X = \ell \left(\frac{t_2 - t_1}{\Delta t_{gage}} \right) \qquad (1)$$

Each AE event was assigned the parameters (i.e. duration, rise time, counts, energy, and amplitude) that were recorded at the first sensor hit.

Spatial filtering of AE events through post-test data reduction was performed to analyze AE events at specified locations along the length of the specimen as well as to screen out unwanted AE events from the grips. Unless noted, all AE events outside -85% to 85% of the gage length (ℓ = ±30 mm measured from the center of the specimen) were classified as grip noise and thus were screened out.

Results and Discussions

In this section, the application of the AE technique to locate and monitor damage in TMC is demonstrated. The dominant modes of damage were identified and the deformation and AE responses were measured. During static loading, the AE technique was used to locate damage based on the difference in arrival times of the AE event at each sensor. A correlation was established between the major modes of damage and the AE events amplitude in model specimens exhibiting a dominant failure mechanism. Using this correlation, the damage growth process was

monitored in TMC laminates exhibiting multiple modes of damage.

Observed Modes of Damage

The primary modes of damage observed in the SCS-6/β21S specimens tested were matrix plastic deformation, matrix cracking, fiber-matrix debonding and fiber breakage. Each of these failure mechanisms are illustrated in the photomicrographs of the fracture surfaces in the vicinity of the notch of several specimens as shown in Figures 3 through 5.

Ductile rupture of the matrix material was evident in all cases as shown in Figures 3 through 5. In the $[0]_4$ and $[0/90]_s$ specimens, the 0° fibers broke at different lengths and were pulled-out as shown in Figures 3 and 4, respectively. In all lay-ups, fibers were clean of matrix material indicating failure of the fiber-matrix interface. Details of a fracture surface near the interface along a 90° fiber revealed fiber-matrix debonding between the carbon-rich coatings and matrix cracking as shown in Figure 5 for a $[90]_4$ specimen. In addition, the brittle reaction zone (consisting of titanium silicides and titanium carbides) that develops during composite consolidation fractured in a $[0/90]_s$ specimen and a $[90]_4$ specimen, as shown in Figures 4 and 5, respectively.

These damage modes occurred on the interior of the specimen and are thus referred to as non-visual damage. In theory, the deformation process associated with each of these modes of damage will release a characteristic stress wave or AE signal having distinct values of the AE parameters such as the events amplitude. Thus, the AE technique may offer an effective NDE method to determine the both the occurrence and identification of non-visual damage in real-time as discussed in the subsequent sections.

Deformation and AE Responses

The global displacements measured using an extensometer with a 25.4-mm gage length and the accumulative number of AE events as a function of the applied stress are shown in Figures 6 through 9 for both a neat β21S specimen and several TMC specimens. In general, as shown in these figures, the AE activity initiated early in the loading history indicating the occurrence of

damage. Then the number of AE events increased substantially as the ultimate load was approached.

In the unnotched β21S specimen, the AE events initiated at a stress level of approximately 700 MPa which could be associated with localized matrix plastic deformation, Figure 6. Once the proportional limit was reached at approximately 950 MPa (determined visually and defined in this study as the point of nonlinearity of the initial portion of the stress-strain curve), the number of AE events substantially increased.

The effect of notch geometry on the deformation and AE response in $[0]_4$ SCS-6/β21S is apparent by comparing the responses of center notch and center hole specimens, Figures 7 and 8, respectively. In the center hole specimen, Figure 8, the deformation response is nearly linear. Catastrophic fracture was sudden, without AE warning (i.e., no sudden increase in the number of AE events). In the center notched specimen, Figure 7, a sharp increase in the AE activity and a corresponding jump in the global displacement are evident prior to fracture, both indicating the occurrence of damage. Moreover, the notched strengths, S_{ult}, for the two specimens were similar despite the large difference in the stress concentration factors for both. For the center hole specimen, $K_t = 3.58$ and $S_{ult} = 894$ MPa, and for the center notched specimen, $K_t = 10$ and $S_{ult} = 912$ MPa. Similar observations were obtained comparing the notched strength of double edge notched (DEN) and center hole specimens of $[0/90]_{2s}$ SCS-6/Ti-15-3 [15]. Fiber-matrix debonding along the first intact 0° fiber was evident only in the DEN specimen which caused a reduction in stress concentration. In the center hole specimen, no such stress relief mechanism was observed, thus the notched strengths for the two specimens were similar.

The effect of lay-up on the deformation and AE response of SCS-6/β21S is shown by comparing the responses of $[0]_4$ and $[0/90]_s$ center notched specimens, Figures 7 and 9, respectively. The total global displacements to failure were similar for both lay-ups (approximately 145 μm). However, the notched strength, S_{ult}, was approximately 40% higher for the $[0]_4$ specimen than for the $[0/90]_s$ specimen and the AE responses for both specimens were significantly different. In the $[0]_4$ specimen, the rate of acoustic emission continuously increased

with increase in applied load up to failure, Figure 7. In the $[0/90]_s$ specimen, the number AE events recorded was approximately four times greater than that for the $[0]_4$ specimen. The rate of emission increased with increase in load, however, the rate of increase began to decline at a nominal applied stress level of approximately 222 MPa (40% of S_{ult} = 555 MPa), Figure 9. The majority of the AE events recorded up to this stress level is associated with damage occurring in the 90° plies as discussed later. When the nominal applied stress approached the ultimate stress, the rate of emission again increased, Figure 9.

Location of Damage

The location of damage was determined from the difference in the arrival times of the AE event at each sensor. Damage and, hence, AE activity will be more pronounced in the vicinity of a stress concentration. Figure 10 shows location distribution histograms (LDH) for a center notched $[0]_4$ specimen at various stages of quasi-static loading to failure. Initially, the AE events recorded along the length of the specimen could be attributed to local matrix plastic deformation and fiber-matrix debondings. A distinct peak of AE events occurred along the plane of the center notch at a nominal stress level of approximately 600 MPa. As the nominal stress level was increased, the amount of AE activity increased in the notch area, the location of final fracture. Similar characteristics were observed in the LDH for a center notched $[90]_4$ specimen, Figure 11. Both figures show a distinct peak of AE events in the notch region where final fracture occurred.

The LDH for a center notched $[0/90]_s$ SCS-6/β21S specimen at various stages of quasi-static loading to failure is shown in Figure 12. There was a peak of AE events in the vicinity of the notch, however, this peak was not as distinctive as in the $[0]_4$ SCS-6/β21S specimen, Figure 10. In the $[0/90]_s$ SCS-6/β21S specimen, the AE events recorded throughout the length were due primarily to wide spread fiber-matrix debonding in the 90° plies as discussed later. Thus, the LDH for the $[0/90]_s$ specimen, Figure 12, is more dispersed than in the $[0]_4$ specimen, Figure 10.

For the center hole $[0]_4$ SCS-6/β21S specimen, the LDH was quite dispersed showing no distinctive peak in the AE events, Figure 13. In this specimen, catastrophic fracture was quite sudden with no stable damage growth from the center hole as revealed by the nearly linear

response of load-displacement curve, Figure 8 and as observed using the CCTV. The AE equipment was unable to record the AE events associated with the sudden damage growth in this specimen and thus failed to detect its location. Similar results were obtained in [9] where the AE technique was unable to detect damage in Boron/Aluminum specimens containing small initial notch lengths ($2a/W < 0.1$) in which sudden catastrophic fracture occurred. Damage was easily and repeatedly located in specimens containing longer crack lengths ($2a/W > 0.2$) where a slower and more stable damage growth processes occurred [9].

The LDH of a center hole $[0/90]_{2s}$ SCS-6/β21S specimen during a post-fatigue static test is shown in Figure 14. This specimen was subjected to a prior fatigue loading for 300,000 cycles at an applied load of S_{max} = 150 MPa and a stress ratio of R = 0.1. Under these fatigue loading conditions, matrix cracks progressed from the center hole normal to the 0° fibers. These matrix cracks were bridged by intact 0° fibers. As the matrix cracks grow past the 0° fibers, fiber-matrix debonding is assumed to occur based on the observed relative displacement between the bridging fibers and the matrix crack surfaces. As shown in Figure 14, a V-shaped LDH was obtained for this specimen when it was loaded statically to failure. It is believed that fewer events were recorded in the center of the specimen due to the existing fatigue damage state in this region consisting of fiber-matrix debonding (in the 90° plies and 0° plies) and matrix cracking. The AE events associated with this damage state were not recorded. Since damage creates emission one time, the events recorded in the damaged region could be associated with friction generated emission due to grating among the fracture surfaces. Events could have been generated from the extension of the debonds of the bridging 0° fibers. In addition, AE events due to fiber-matrix debonding in the 90° plies throughout the specimen length could have also contributed to the V-shaped LDH.

Correlation Between AE Events Amplitude and Observed Modes of Damage

Tests were conducted on model specimens exhibiting dominant modes of damage as summarized in Table 1. The AE result for each of these specimens were analyzed to determine the

correlation between the AE events amplitude and the observed modes of damage, namely, matrix plastic deformation, matrix cracking, fiber-matrix debonding and fiber breakage. An amplitude distribution histogram (ADH) of the AE events for each specimen was generated. From the ADH, a correlation was established between the major modes of damage and the AE results. It should be reemphasized that only qualitative analysis were performed and no attempt was made to quantify the AE results. Thus, the correlations established in this section should not be considered one to one correspondences. It is assumed in each test that the majority of the AE events having the specified amplitude ranges were generated by the corresponding failure mechanisms. Obviously there can be overlap in the AE event amplitudes associated with the various failure mechanisms.

Matrix Plastic Deformation

Deformation of an isotropic material, in this case the matrix, is associated with a variety of mechanisms such as dislocation movement, void coalescence, ductile microrupture, and microcracking. In this study, these mechanisms are generalized in one term as matrix plastic deformation. The correlation between the AE events amplitude and matrix plastic deformation was established using an unnotched neat β21S specimen loaded quasi-statically to failure. The corresponding ADH is shown in Figure 15. No events were recorded below 40 dB since this was the selected system threshold. Most of the AE events recorded had amplitudes below 60 dB and are thus associated primarily with matrix plastic deformation.

Matrix Cracking

A correlation was established between matrix cracking and the AE event amplitude using a center notched neat β21S specimen loaded quasi-statically to failure. The corresponding ADH is shown in Figure 16. Stable matrix cracking and matrix plastic deformation were observed in this specimen. Matrix plastic deformation occurred at the crack-tip as the load increased. As shown in the ADH, AE events having amplitudes below 60 dB (low amplitude events) were recorded. Based on the results for the unnotched specimen, Figure 15, matrix plastic deformation was associated with the majority of these low amplitude events. In addition, a significant number of

AE events with amplitudes between 60dB and 80dB (middle range amplitude events) were recorded. The time at which these middle range amplitude events were recorded coincided with the time at which stable tearing of the specimen was observed using the CCTV. Thus, matrix cracking was assumed to have generated the majority of these middle range amplitude events.

Fiber-Matrix Debonding

Fiber-matrix debonding is a complex process due to the structure of the interface region. The SCS-6 fiber is manufactured by applying silicon and carbon (SiC) onto a carbon core substrate using a chemical vapor deposition (CVD) process. Then two carbon-rich coatings are applied to the SiC fiber. During composite consolidation, a brittle reaction zone forms between the outer carbon-rich coating and the titanium matrix. This reaction zone consists of brittle titanium silicides and titanium carbides [18]. The resulting fiber-matrix interface is composed of two carbon-rich coatings and a brittle reaction zone. Fiber-matrix debonding in TMC consists of fracture of the brittle reaction zone and cracking between the two carbon-rich coatings [19].

Transverse $[90]_4$ SCS-6/β21S specimens were used to determine the correlation between the AE events amplitude and fiber-matrix debonding. An unnotched specimen was loaded incrementally in tension up to failure. Catastrophic fracture of this specimen occurred outside the sensor gage length. At several load levels, edge replicas were taken. Post-test examinations of the edge replicas revealed that fiber-matrix debonding had occurred at a nominal applied stress level of 240 MPa. Photographs of the edge replicas made using an SEM are shown in Figure 17. As shown in this figure, the SiC fiber and the first carbon rich coating are protruded indicating fiber-matrix debonding between the two carbon-rich coatings. The corresponding ADH (up to is a stress level of 240 MPa) is shown in Figure 18. As shown in the ADH, middle range amplitude events, amplitudes between 60dB and 80dB, and low range amplitude events, amplitudes below 60 dB, were recorded. The majority of the low amplitude events are assumed to be generated by localized matrix plastic deformation. Since no other failure mechanism was activated, fiber-matrix debonding is assumed to be associated with the majority of the middle range amplitude events.

Cracking of Reaction Zone

The unnotched $[90]_4$ SCS-6/β21S specimen failed outside of the sensor gage length. Thus, only the AE events associated with the onset of fiber-matrix debonding are shown in Figure 18. In order to record the AE events associated with specimen fracture, a center notched $[90]_4$ SCS-6/β21S specimen was tested. Failure occurred in the net section along the plane of the center notch. The corresponding ADH is shown in Figure 19. As shown in this figure, low and middle range amplitude events were recorded and were assumed to have been generated mainly by matrix plastic deformation and fiber-matrix debonding, respectively. Upper-middle range amplitude events, amplitudes between 80 dB and 99 dB, were also recorded. Photomicrographs of the specimens fracture surface taken using the SEM is shown in Figure 5. The closer detail of the interface region shown in the figure reveals fracture of the brittle reaction zone and cracking of the surrounding matrix. It is assumed that the former will generate upper-middle range amplitude events since the reaction zone is brittle. The matrix cracking will generate middle range amplitude events based on the results of the notched β21S specimen, Figure 16. In addition, the dimpled texture of the fracture surface of the matrix shown in Figure 5, indicates matrix plastic deformation which generated mainly low amplitude events.

Fiber Breakage

Fiber breakage is a critical mode of damage in TMC. Catastrophic fracture of the specimen is usually imminent at the onset of fiber breakage. Residual strength predictions have been developed based on the initiation of fiber fracture [15,16]. Thus, knowing when fibers break is quite important. The AE technique is ideally suited to monitor fiber breaks due to the distinctive stress wave emitted during fiber breakage. It has been well established that fiber breakage in Boron/Aluminum (B/Al) is associated with high amplitude events [9,10,17]. An excellent correlation was established between the number of high amplitude events and the number of fiber breaks in unidirectional B/Al [17]. In addition, it was reported that fracture of individual boron fibers were also associated with high amplitude events [10].

In the current study, a correlation between the AE results and fiber breakage was determined using a center notched, unidirectional $[0]_4$ SCS-6/β21S specimen. The specimen was loaded quasi-statically until high amplitude events were recorded (that is, up to a nominal applied stress of 750 MPa). The ADH for this specimen is shown in Figure 20. Results indicated that the number of events greater than 99 dB was similar to the number of fiber breaks. A total of 8 AE events greater than 99 dB were recorded. The matrix material was removed from the specimen, and 5 broken fibers were found in the exterior plies along the notch center-line. Assuming that the same number of broken fibers would occur in the interior plies as in the exterior plies, a total of 10 broken fibers was estimated. Thus, an excellent correlation was established between high amplitude events and fiber breakage

The correlation between the high amplitude events and fiber breakage was further verified using a cross-ply $[0/90]_{2s}$ SCS-6/β21S specimen subjected to fatigue loading. A total number of 105 high amplitude events were recorded. After removing the outer layer of matrix material, 55 broken fibers were found in the exterior plies. A total of 110 broken fibers was estimated by assuming that the same number of fibers broke in the interior plies.

In practically all cases, fiber breaks were successfully located by AE events with amplitudes greater than 99 dB (high amplitude events). The LDH of the high amplitude events for several cases are shown in Figure 21. As shown in this figure, distinct peaks of events are evident along the center-line of the notch or hole where the final fractures occurred. Of particular interest is the LDH for the center hole $[0/90]_{2s}$ specimen subjected to the prior fatigue loading history. When all the events were considered, the corresponding LDH had a distributed V-Shape thus giving no indication of where final fracture took place, Figure 14. However, when considering the events associated with fiber breakage, the LDH revealed a peak of events at the notch center-line where final fracture occurred, Figure 21d.

Monitoring Damage Growth

Having established a correlation between the AE events amplitude and the dominant modes of damage as summarized in Table 1, the damage growth process was monitored in several laminates. The AE events of several amplitude ranges and the global displacement are plotted as a function of stress for selected center notched cases in Figures 22, 23 and 24. Also shown in these figures are schematics of the damage growth process interpreted from the AE results. In general, as the applied load increased, low amplitude events were generated first, followed by middle range, upper-middle range and then high amplitude events. It should be noted that there is overlap in the AE event amplitudes associated with the various failure mechanisms as discussed previously.

For the $[0]_4$ specimen, low amplitude events were generated first at approximately 9% of the notched strength, S_{ult} = 912 MPa; these low amplitude events are associated with matrix plastic deformation near the notch-tip, Figure 22. Middle range amplitude events were then recorded as the load increased (initiating at approximately 25% of the notched strength) and were assumed to be generated mainly by fiber-matrix debonding. Virtually no upper-middle range amplitude events were recorded. The high amplitude events coincided with jumps or sudden increments in the global displacement at the high loads. These high amplitude events are associated with fiber breakage (initiated at approximately 88% of the notched strength). Note that the number of low and middle range amplitude events had a sharp increase at the same load level at which the majority of the high amplitude events were recorded. Following a fiber break, localized matrix plastic deformation and fiber-matrix debonding in the vicinity of the fiber break would produce an increase in the low and middle range amplitude events, respectively. Photomicrographs of the fracture surface near a broken fiber reveal the ductile dimple-like fracture surface of the matrix material and fiber-matrix debonding due to fracture of the carbon-rich coatings, Figure 3. Note that for all three amplitude ranges, the rate of emission tended to increase as the applied load increased.

For the $[90]_4$ specimen, low amplitude events associated with localized matrix plastic deformation initiated at approximately 41% of the notched strength, S_{ult} = 170 MPa, Figure 23. At this load, the global displacement-stress curve had deviated from linearity. Middle range amplitude events attributed mainly to fiber-matrix debonding were first recorded at approximately 59% of the notched strength. At a higher load (approximately 82% of the notched strength), upper-middle range amplitude events mainly due to cracking of the brittle reaction zone were recorded. A noticeable increase in the middle range amplitude events occurred at the same time. The damage growth process depicted by the AE results for the $[90]_4$ specimen begins with localized matrix plastic deformation, followed by fiber-matrix debonding. From the debonded fiber-matrix surface, fracture of the brittle reaction zone occurs which then initiated matrix cracking near the interface. The AE results agree with the photomicrographs in Figure 5 that reveal fracture of the brittle reaction zone and matrix cracking close to the interface. Note that for all three amplitude ranges, the rate of emission tends to increase as the applied load increases.

For the $[0/90]_s$ specimen, the initiation of low, middle and upper-middle amplitude events occurred at approximately 9%, 22% and 29% of the notched strength, S_{ult} = 555 MPa, Figure 24. The rate of emission of the events in each of these amplitude ranges increased as the stress level increased in the initial stages of loading. At approximately 40% of the notched strength, the rates of emission decreased, particularly for the middle and upper-middle amplitude events. The majority of the AE events generated up to this point are likely to be associated with damage mechanisms occurring in the 90° plies as discussed previously for the $[90]_4$ specimen: matrix plastic deformation, followed by fiber-matrix debonding, and then fracture of the brittle reaction zone. Each of these failure mechanisms are seen in the photomicrographs of the fracture surface, shown previously in Figure 4. Above approximately 40% of the notched strength, the number of upper-middle amplitude range events increased only slightly indicting that damage in the 90° plies is becoming saturated. The majority of AE events generated at loads above 40% of the notched strength are likely to be associated with damage occurring in the outer 0° plies. The occurrence of high amplitude events occurred at approximately 86% of the notched strength and are associated

with fiber breakage. In general, the rate of emission of events in all amplitude ranges increased at the load at which high amplitude events were recorded.

Concluding Remarks

In this study, the viability of the acoustic emission (AE) technique to locate and monitor damage growth in titanium matrix composites (TMC) was addressed. The locations of the AE events between two sensors were determined based on the difference in the arrival times of the events at the sensors. A correlation was established between the dominant failure mechanisms and the AE events amplitude for model specimens which exhibited a dominate failure mechanism. Results revealed that matrix plastic deformation, matrix cracking, and fiber breakage are associated with acoustic emission event amplitude ranges below 60dB (low amplitude events), 60dB to 80dB (middle amplitude events), and over 99dB (high amplitude events), respectively. In addition, fiber-matrix debonding is associated with event amplitudes between 60dB and 80dB (middle amplitude events), while cracking of the reaction zone is associated with event amplitudes between 80dB and 99dB (upper-middle amplitude events). Using the these amplitude ranges, the damage growth process was monitored in center notched $[0]_4$, $[90]_4$, and $[0/90]_s$ laminates exhibiting multiple modes of damage. This study demonstrated the feasibility of the AE technique in small scale laboratory tests to aid in materials characterization.

Acknowledgements

The first author gratefully acknowledges the support extended by the National Research Council, Washington, D.C., through their Associateship Program. Thanks are also due Mr. Scott Willard, Research Engineer, Lockheed Engineering and Sciences Company, Hampton, VA, for obtaining the micrographs using the scanning electron microscope.

References

[1] Pollock, A. A., "Acoustic Emission Inspection," Metals Handbook, Ninth Edition, Volume 17, ASM International, 1989, pp. 278-294.

[2] Michaels, J. E., Michaels, T. E., and Sachse, W., "Applications of Deconvolution to Acoustic Emission Signal Analysis," *Materials Evaluation*, Vol. 39, October 1981, pp. 1032-1039.

[3] Eitzen, D. G., Breckenridge, F. R., Clough, R. B., Fuller, E. R., Hsu, N. N., and Simmons, J. A., "Fundamental Developments for Quantitative Acoustic Emission Measurements," Interim Report for Electric Power Research Institute NP-2089, 1981.

[4] *Acoustic Emission Testing of Aerial Devices and Associated Equipment Used in the Utility Industries*, ASTM STP 1139, A. H. Bingham, C. W. Elkm, and J. R. Tanner, Eds., American Society for Testing and Materials, Philadelphia, 1992.

[5] *Recommended Practice for Acoustic Emission Testing of Fiberglass Reinforced Resin (RP) Tanks/Vessels* The Society of the Plastics Industry, 1987.

[6] *Acoustic Emission Testing,* Nondestructive Testing Handbook, Second Edition, Volume 5, R. K. Miller, and P. McIntire, Eds., American Society for Nondestructive Testing, 1987.

[7] *Proceedings of the Fourth International Symposium on Acoustic Emission From Composite Materials*, Seattle, WA, July 27-31, 1992.

[8] *Proceedings of The 8th International Acoustic Emission Symposium*, Progress in Acoustic Emission III, The Japanese Society of NDI, 1986.

[9] Madhukar, M.S., and Awerbuch, J., "Monitoring Damage Progression in Center- Notched Boron/Aluminum Laminates Through Acoustic Emission," *Composite Materials: Testing and Design (Seventh Conference)*, ASTM STP 893, J.M. Whitney, Ed., American Society for Testing and Materials, Philadelphia, 1986, pp. 337-367.

[10] Awerbuch, J. and Bakuckas J.G., "On the Applicability of Acoustic Emission for Monitoring Damage Progression in Metal-Matrix Composites", in *Metal Matrix Composites: Testing, Analysis and Failure Modes,* ASTM STP 1032, W.S. Johnson, Editor, American Society for Testing and Materials, Philadelphia, 1989.

[11] Awerbuch, J., Madhukar, M., and Gorman, M. R., "Monitoring Acoustic Emission During Quasi-Static Loading/Unloading Cycles of Filament-Wound Graphite/Epoxy Laminate Coupons," *Materials Evaluation*, Vol. 43, No. 6, May 1985, pp. 754-764.

[12] Awerbuch, J., Madhukar, M., and Gorman, M.R., "Monitoring Damage Accumulation in Filament-Wound Graphite/Epoxy Laminate Coupons During Fatigue Loading Through Acoustic Emission," *Journal of Reinforced Plastics and Composites*, Vol. 3, No. 1, January 1984, pp. 2-39.

[13] Awerbuch, J. and Ghaffari, S., "Monitoring Progression of Matrix Splitting During Fatigue Loading Through Acoustic Emission in Notched Graphite/Epoxy Composite", *Journal of Reinforced Plastics and Composites,* Vol. 7, May 1988, pp. 245-264.

[14] Awerbuch, J. and S. Ghaffari, S., "Effect of Friction Emission on Monitoring Damage in Composite Laminates through Acoustic Emission", in the Proceedings of The 8th International Acoustic Emission Symposium, Progress in Acoustic Emission III, The Japanese Society of NDI, 1986, pp. 638-652.

[15] Bigelow, C. A., and Johnson, W. S.,"Effect of Fiber-Matrix Debonding on Notched Strength in Titanium Metal Matrix Composites," *NASA Technical Memorandum 104131*, August 1991.

[16] Bakuckas, J. G. Jr., Johnson, W. S., and Bigelow, C. A.,"Fatigue Damage in Cross-Ply Titanium Metal Matrix Composites Containing Center Holes," *NASA TM 104197*, February 1992.

[17] Johnson, W. S., Bigelow, C. A., and Bahei-El-Din, Y. A.,"Experimental and Analytical Investigation of the Fracture Process of Boron/Aluminum Laminates Containing Notches," *NASA Technical Paper 2187*, 1983.

[18] Naik, R. A., Pollock, W. D., and Johnson, W. S.,"Effect of a High-Temperature Cycle on the Mechanical Properties of Silicon Carbide/Titanium Metal Matrix Composites," *Journal of Materials Science*, Vol. 26, 1991, pp. 2913-2920.

[19] Bakuckas, J. G., Jr., and Johnson, W. S.,"Application of Fiber Bridging Models to Fatigue Crack Growth in Unidirectional Titanium Metal Matrix Composites," *NASA Technical Memorandum 107588*, July 1992.

Table 1. Correspondence between the dominant modes of damage and AE events amplitude

Specimen Type	Dominant Mode of Damage	AE Event Amplitude (dB)
Unnotched β21S	Matrix Plastic Deformation	Below 60 dB (Low Amplitude)
Center Notched β21S	Matrix Cracking	60 dB to 80 dB (Middle Amplitude)
Unnotched $[90]_4$ SCS-6/β21S	Fiber-Matrix Debonding	60 dB to 80 dB (Middle Amplitude)
Center Notched $[90]_4$ SCS-6/β21S	Cracking of Brittle Reaction Zone	80 dB to 99 dB (Upper-Middle Amplitude)
Center Notched $[0]_4$ SCS-6/β21S	Fiber Breakage	Above 99 dB (High Amplitude)

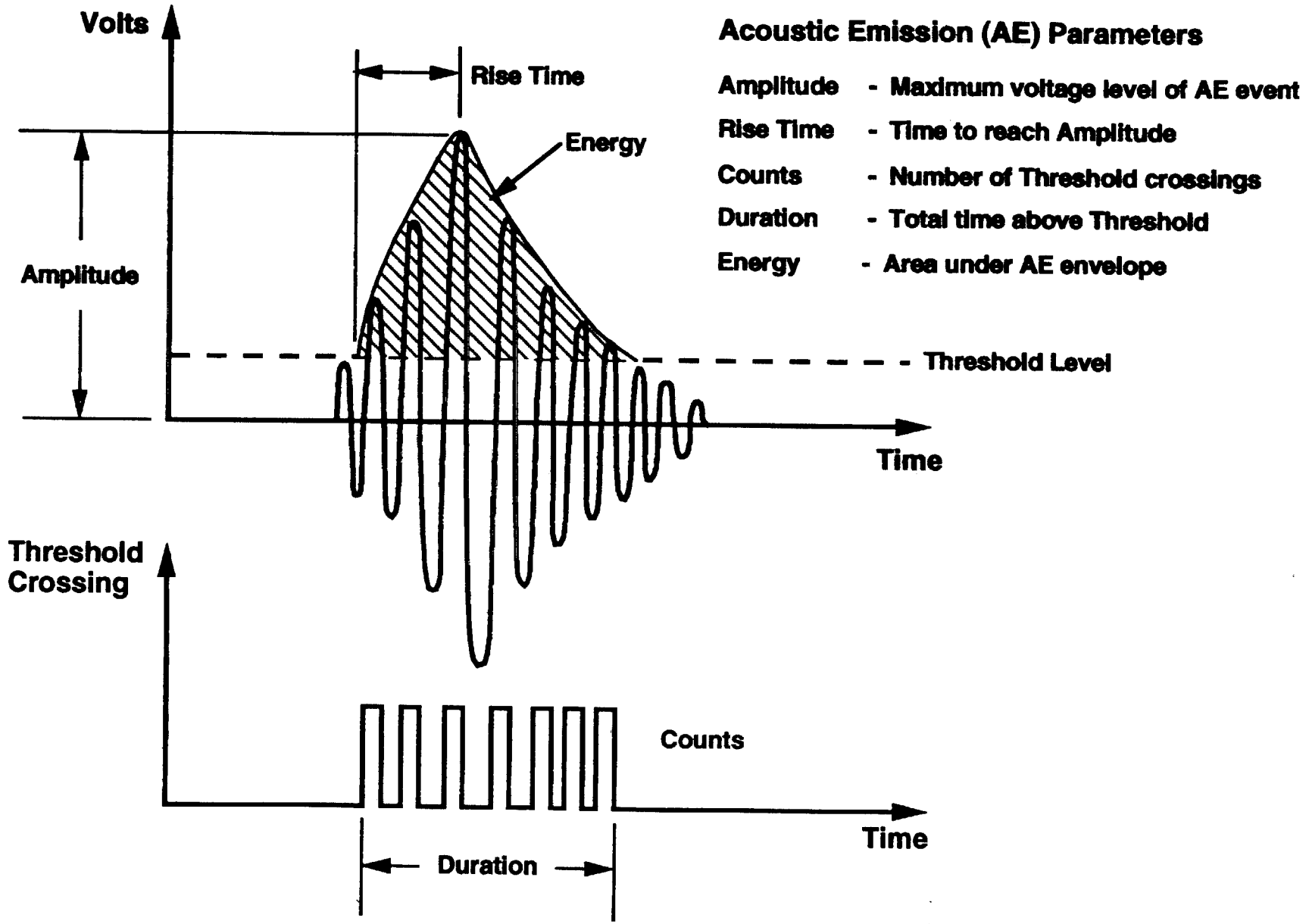

Figure 1. Acoustic Emission (AE) event definitions.

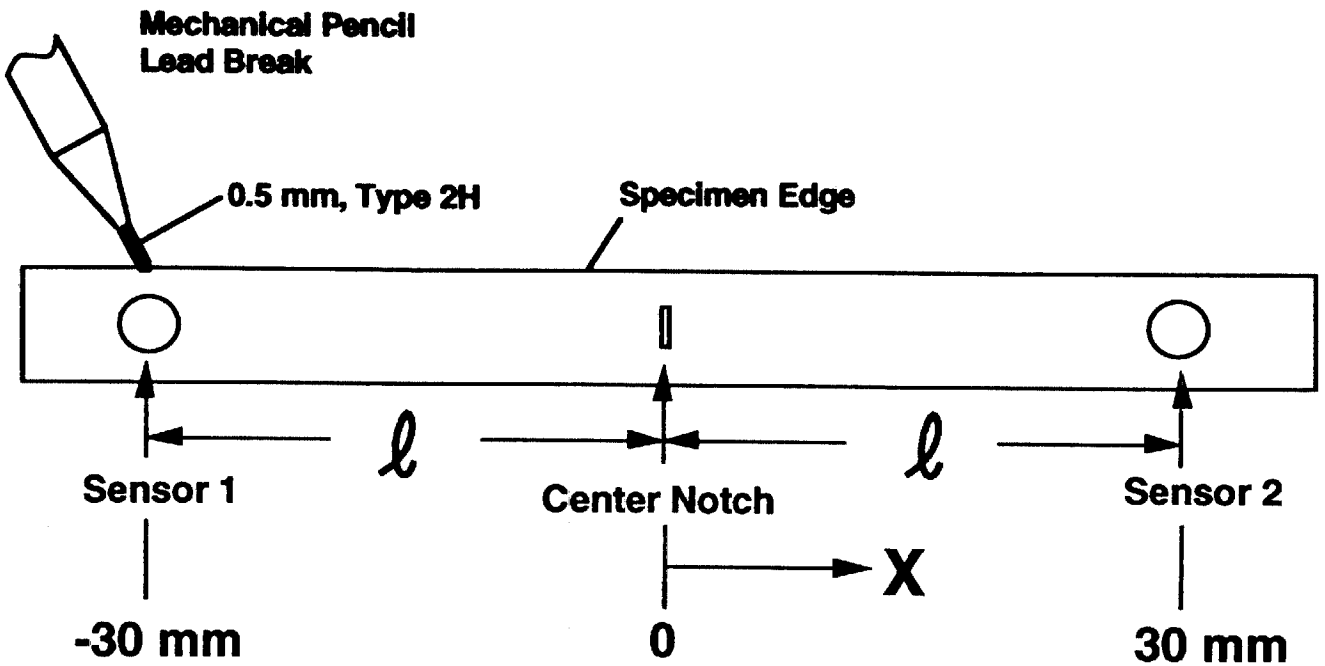

Figure 2. Hsu mechanical pencil lead break used for location calibration.

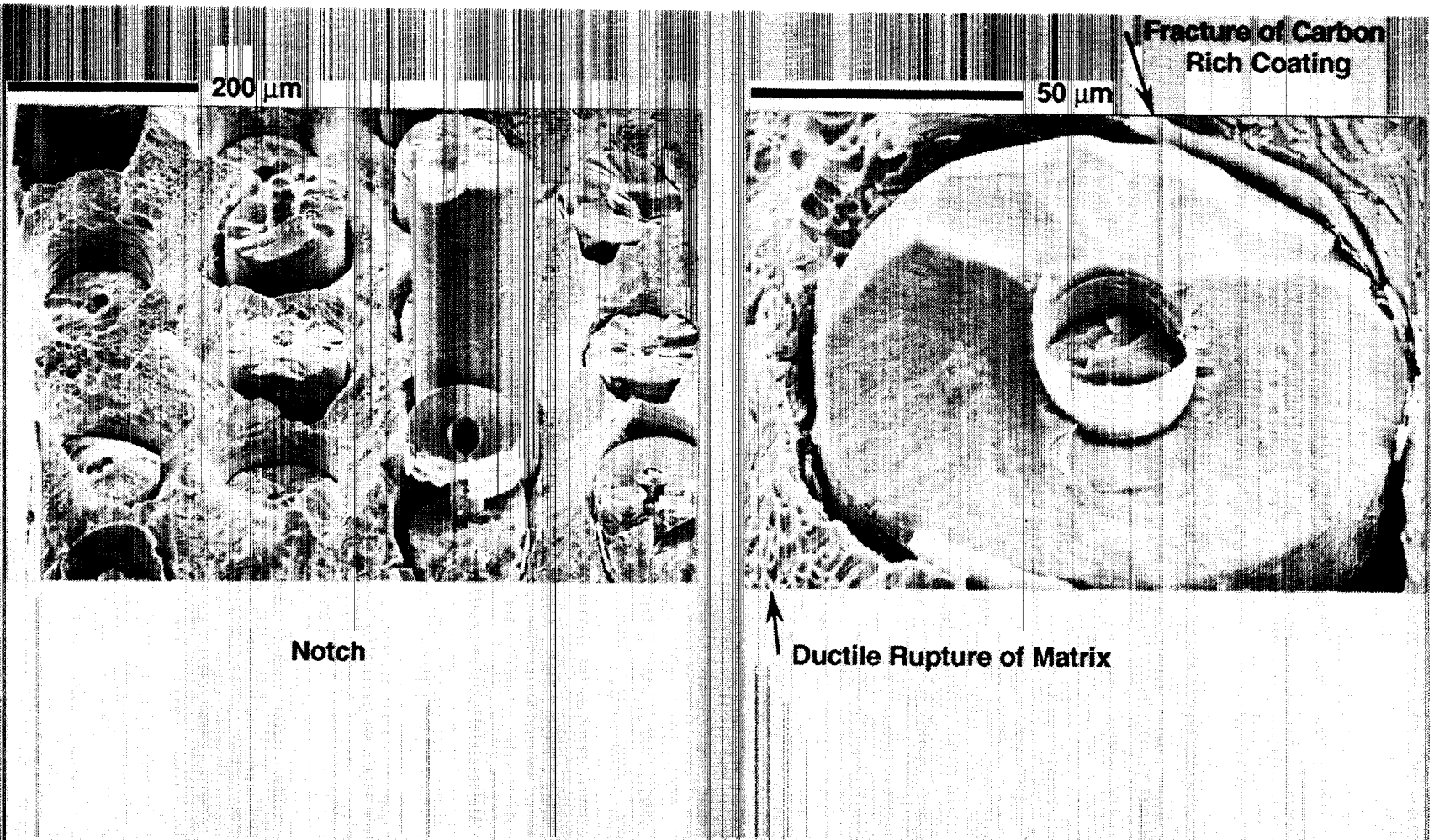

Figure 3. Photomicrographs of the fracture surfaces of a center notched $[0]_4$ SCS-6/β21S specimen showing ductile rupture of the matrix and cracking of the carbon coating near a broken fiber.

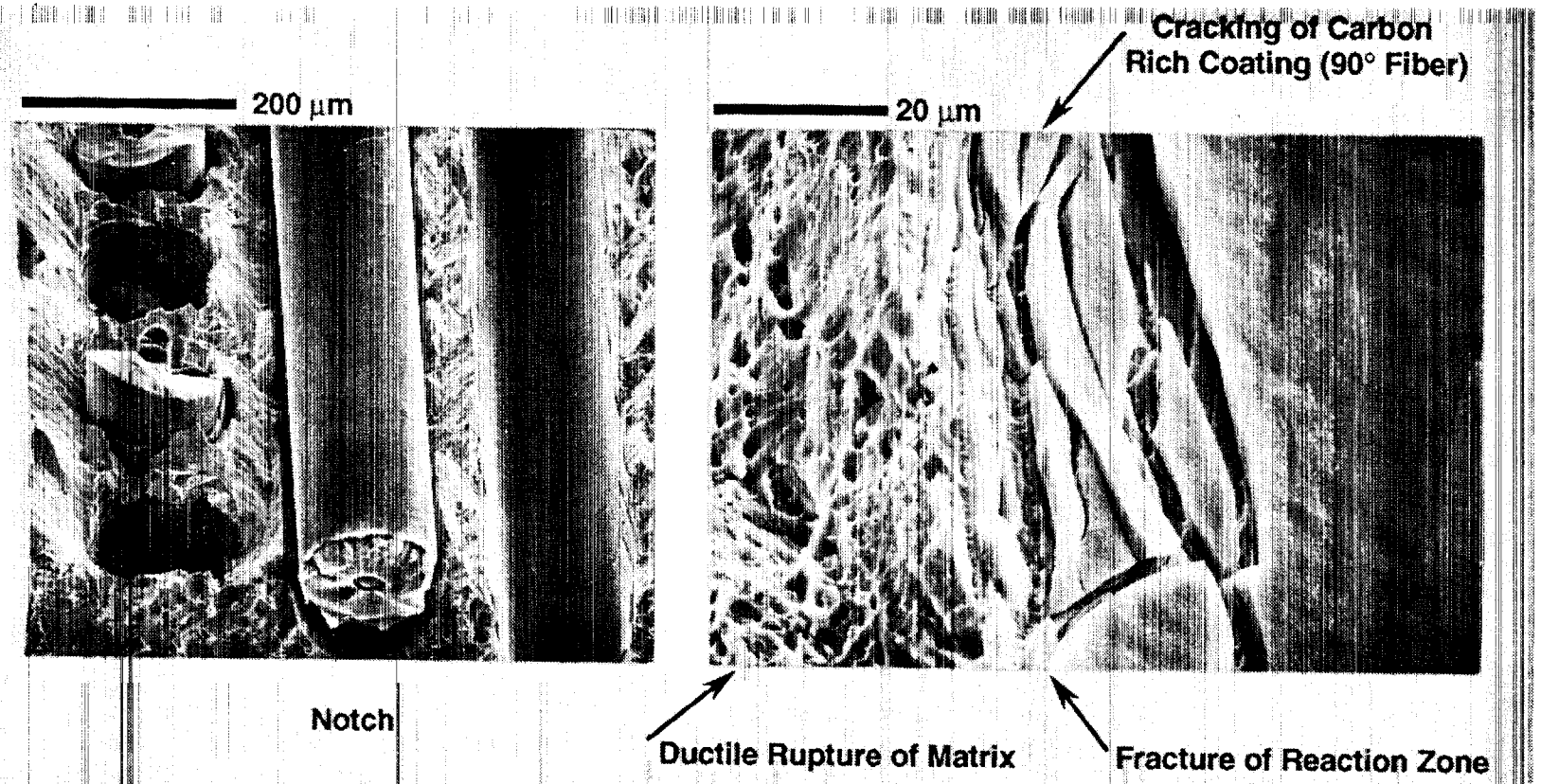

Figure 4. Photomicrographs of the fracture surfaces of a center notched $[0/90]_s$ SCS-6/β21S specimen showing ductile rupture of the matrix, cracking of the carbon coating, fracture of the brittle reaction zone, and fiber breakage.

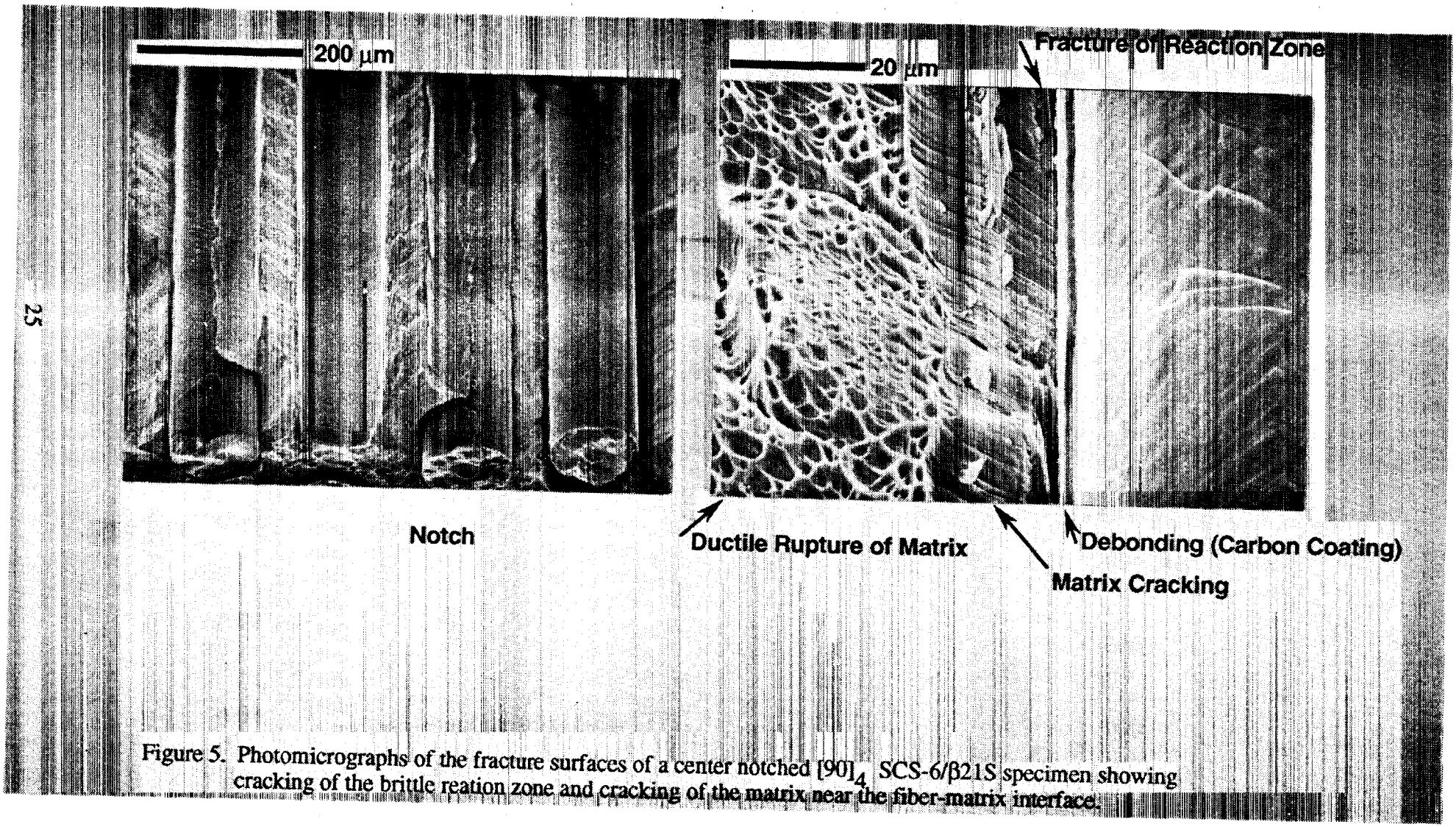

Figure 5. Photomicrographs of the fracture surfaces of a center notched $[90]_4$ SCS-6/β21S specimen showing cracking of the brittle reation zone and cracking of the matrix near the fiber-matrix interface.

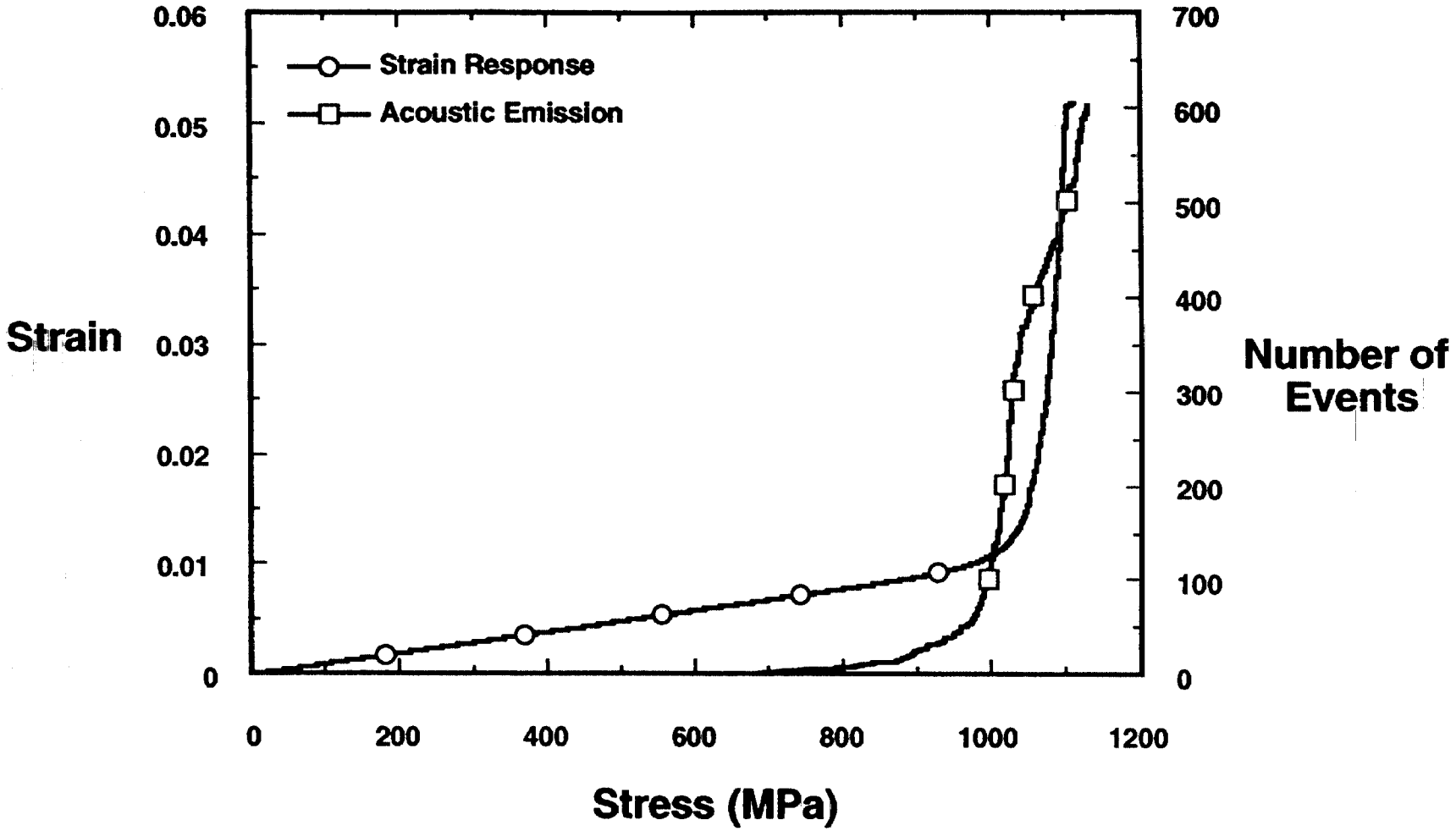

Figure 6. Deformation and AE response of unnotched neat β21S specimen during static loading.

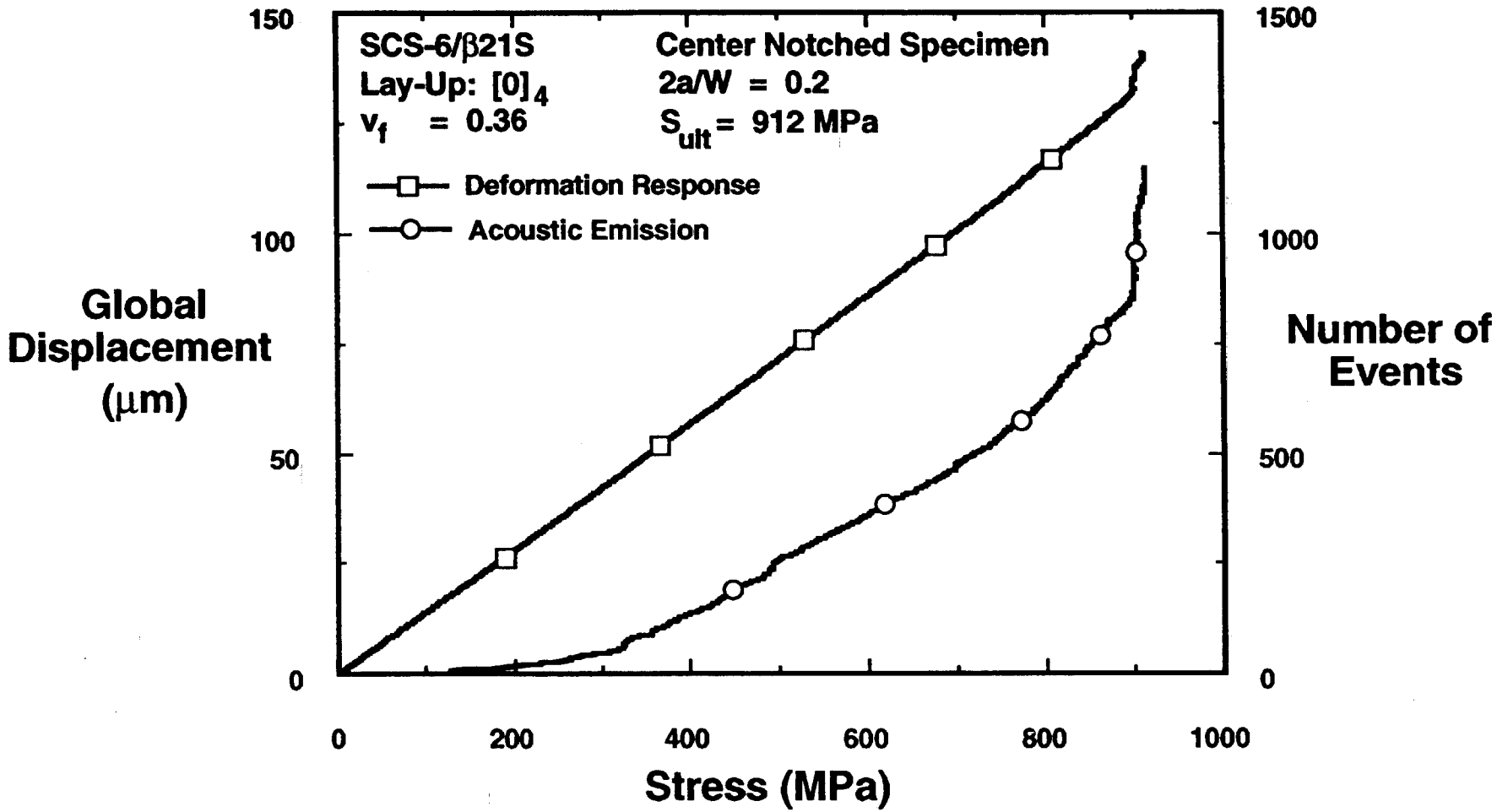

Figure 7. Deformation and AE response of center notched $[0]_4$ SCS-6/β21S specimen during static loading.

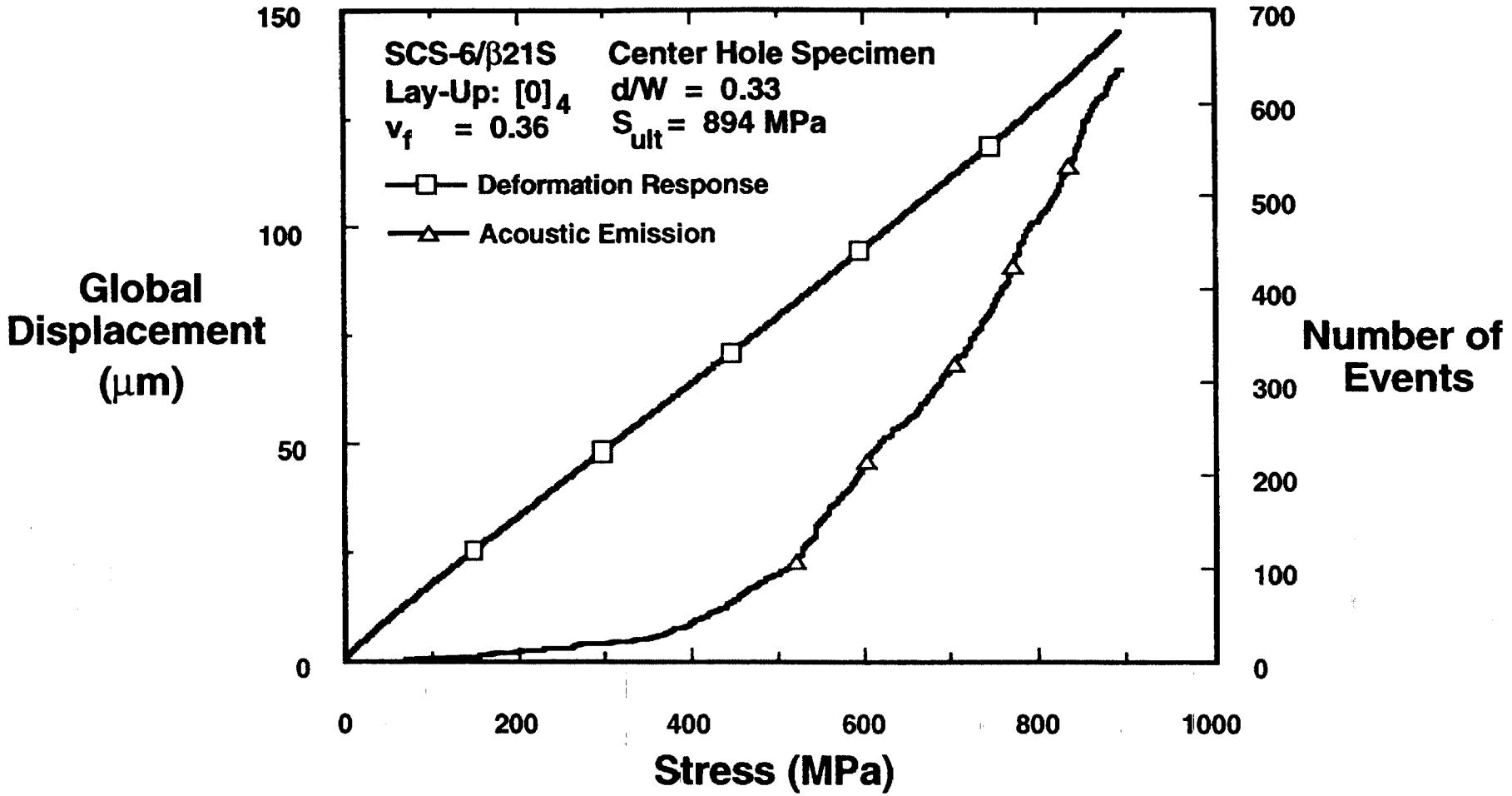

Figure 8. Deformation and AE response of center hole $[0]_4$ SCS-6/β21S specimen during static loading.

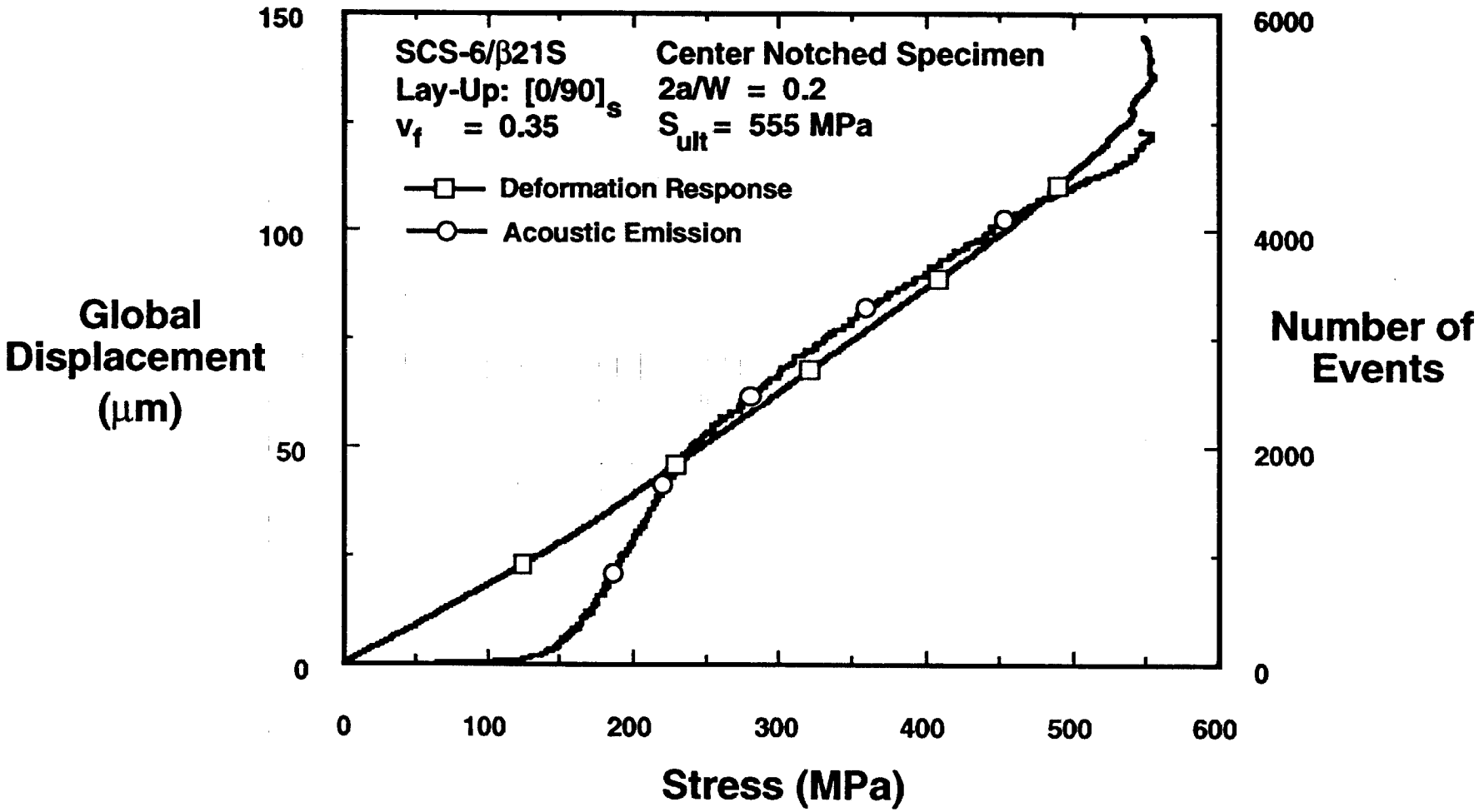

Figure 9. Deformation and AE response of center notched $[0/90]_s$ SCS-6/β21S specimen during static loading.

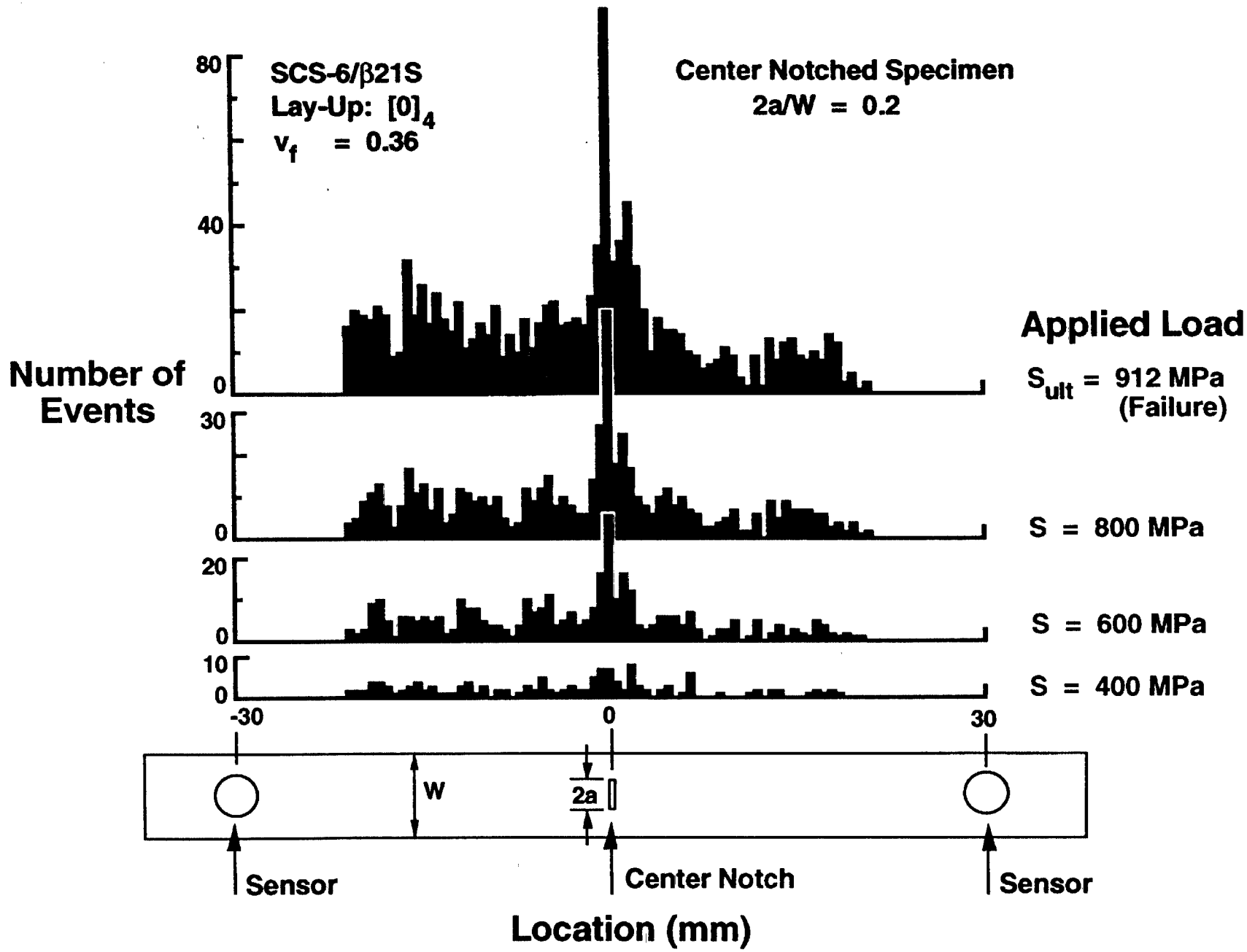

Figure 10. Location distribution histogram of events generated between two sensors on a center notched $[0]_4$ SCS-6/β21S specimen during static loading.

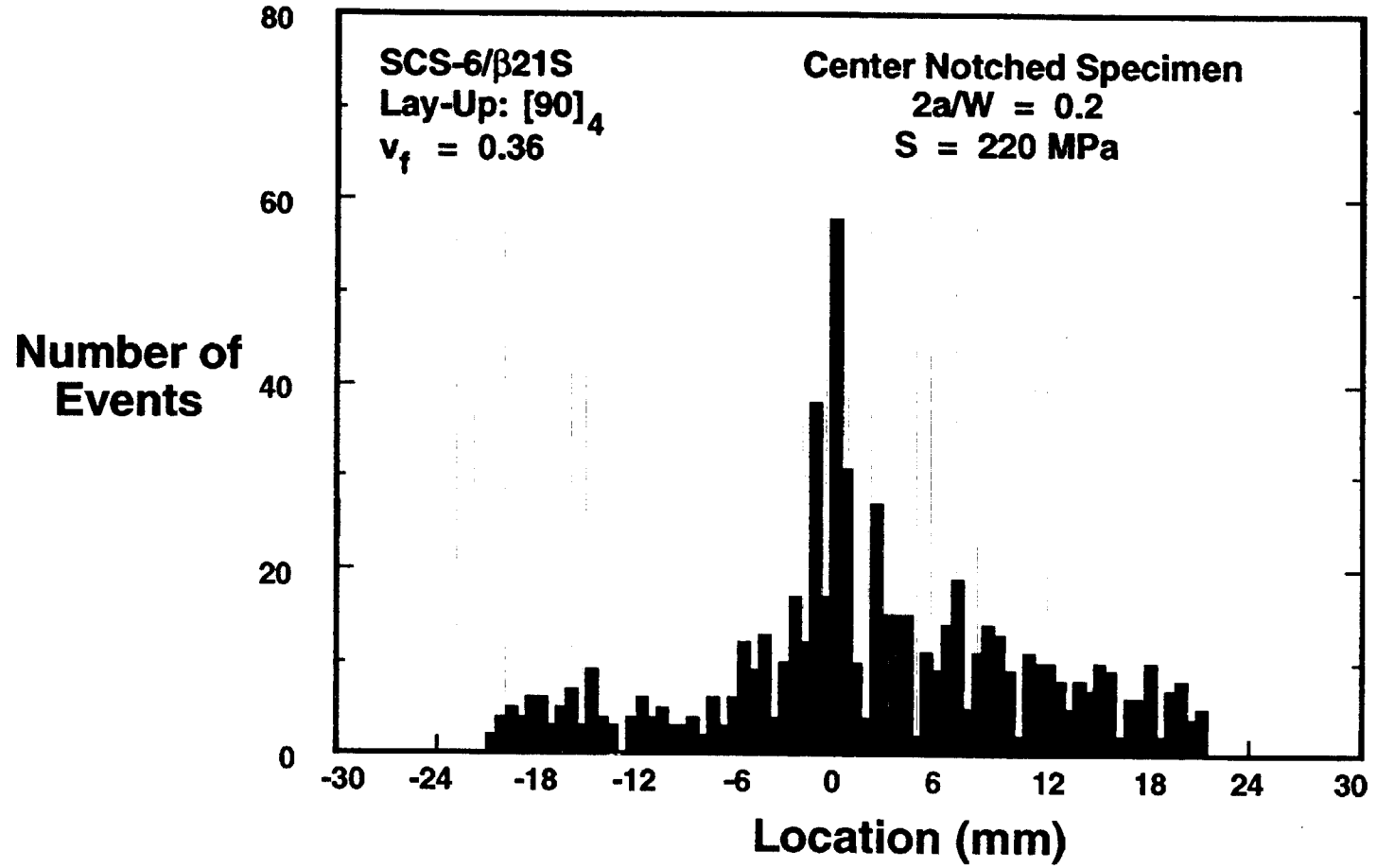

Figure 11. Location distribution histogram of events generated between two sensors on a center notched $[90]_4$ SCS-6/β21S specimen during static loading.

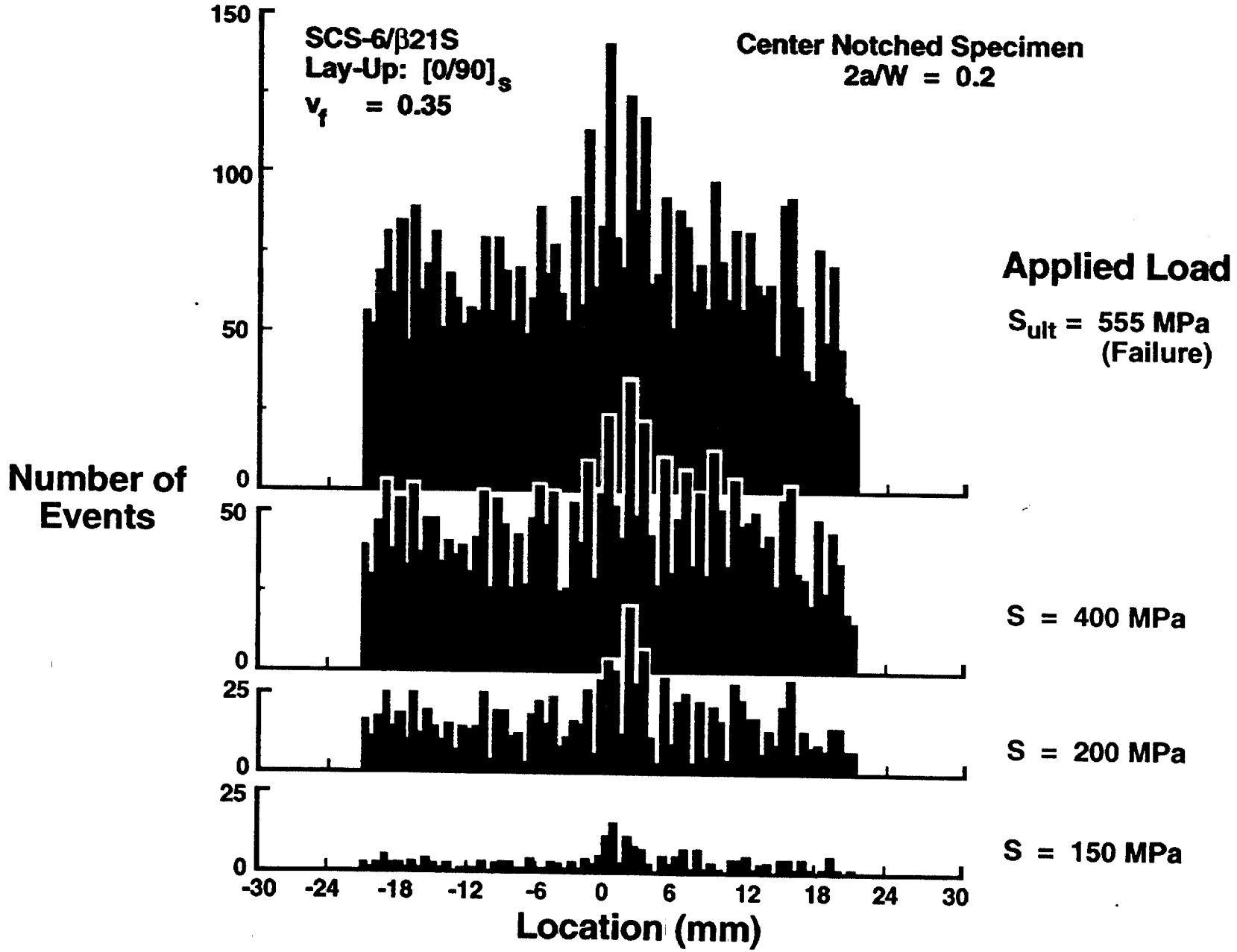

Figure 12. Location distribution histogram of events generated between two sensors on a center notched $[0/90]_s$ SCS-6/β21S specimen during static loading.

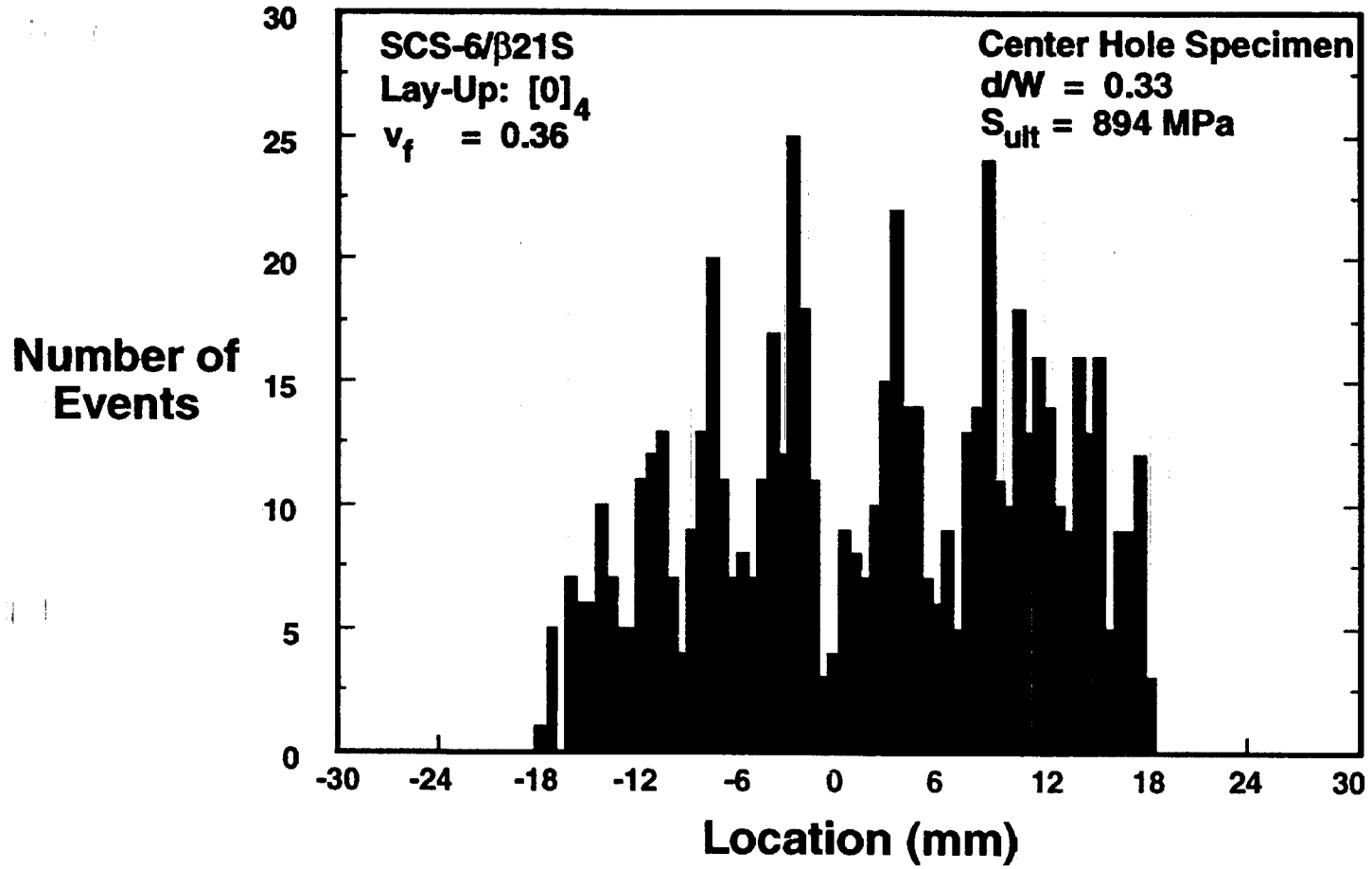

Figure 13. Location distribution histogram of events generated between two sensors on a center hole $[0]_4$ SCS-6/β21S specimen during static loading.

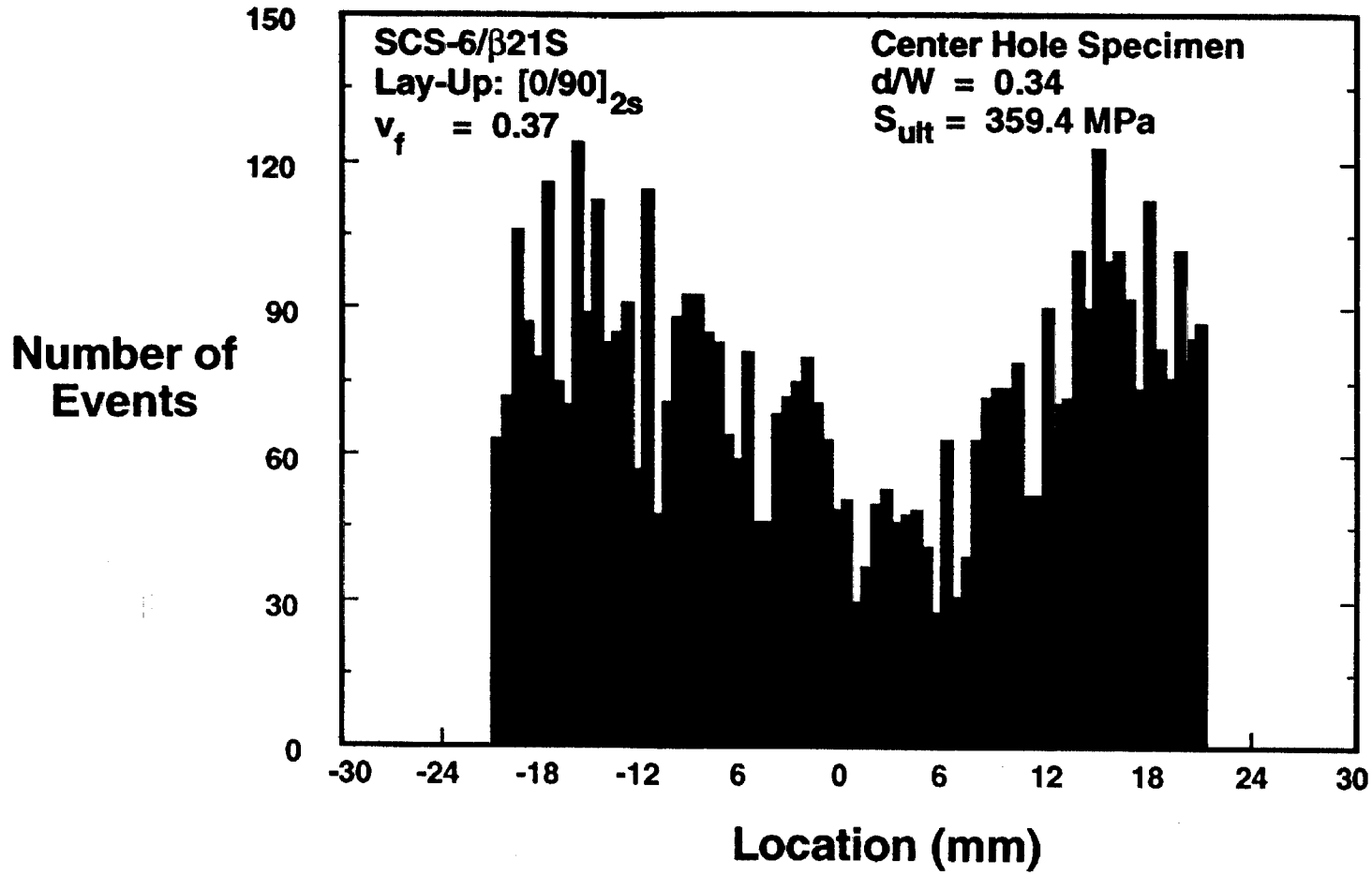

Figure 14. Location distribution histogram of events generated between two sensors on a center hole $[0/90]_{2s}$ SCS-6/β21S specimen subjected to a prior fatigue loading: S_{max}= 150 MPa, R = 0.1, frequency = 10 Hz, N = 300,000 cycles.

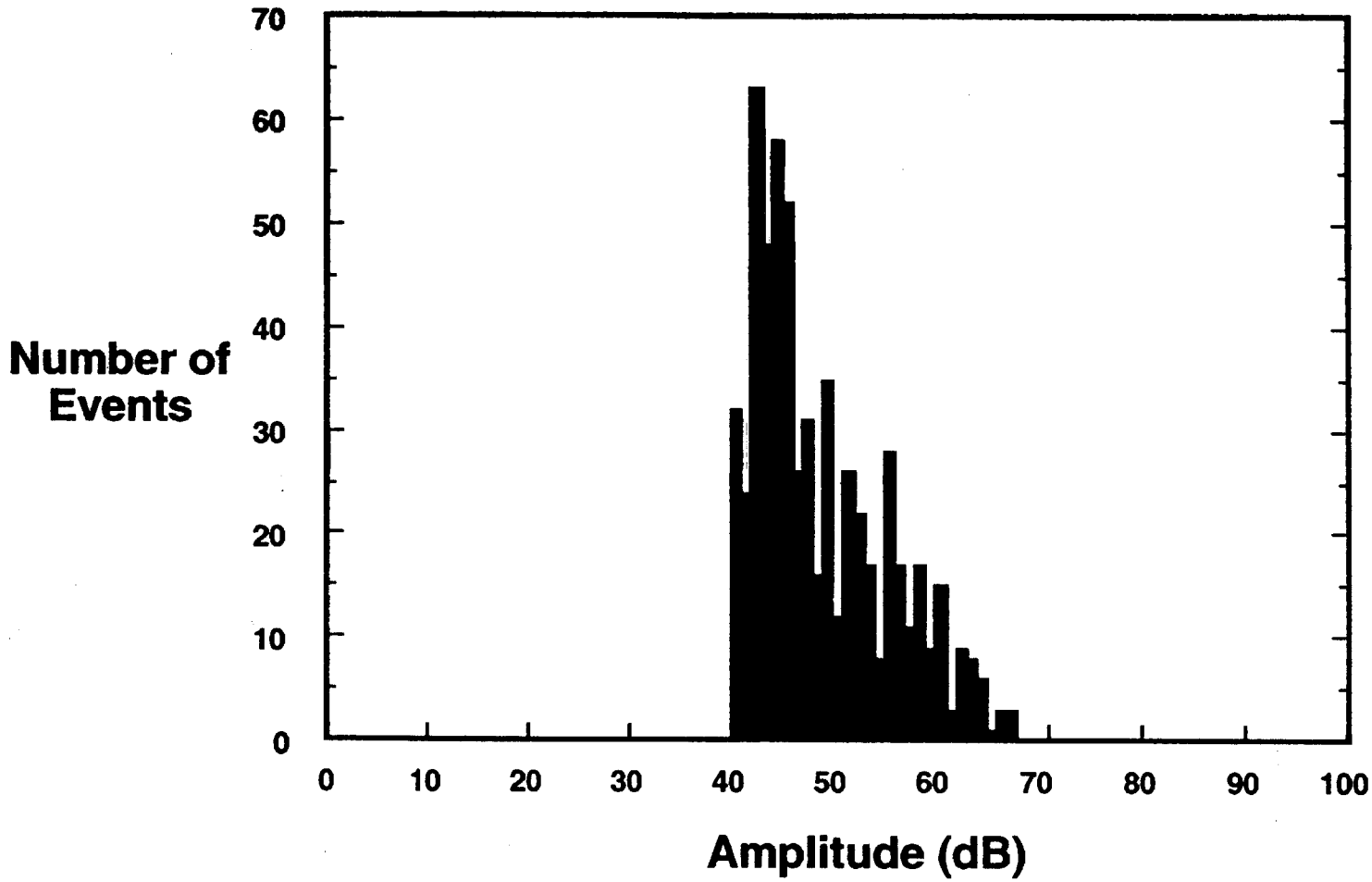

Figure 15. Amplitude distribution histogram of events generated between two sensors on an unnotched β21S specimen during static loading.

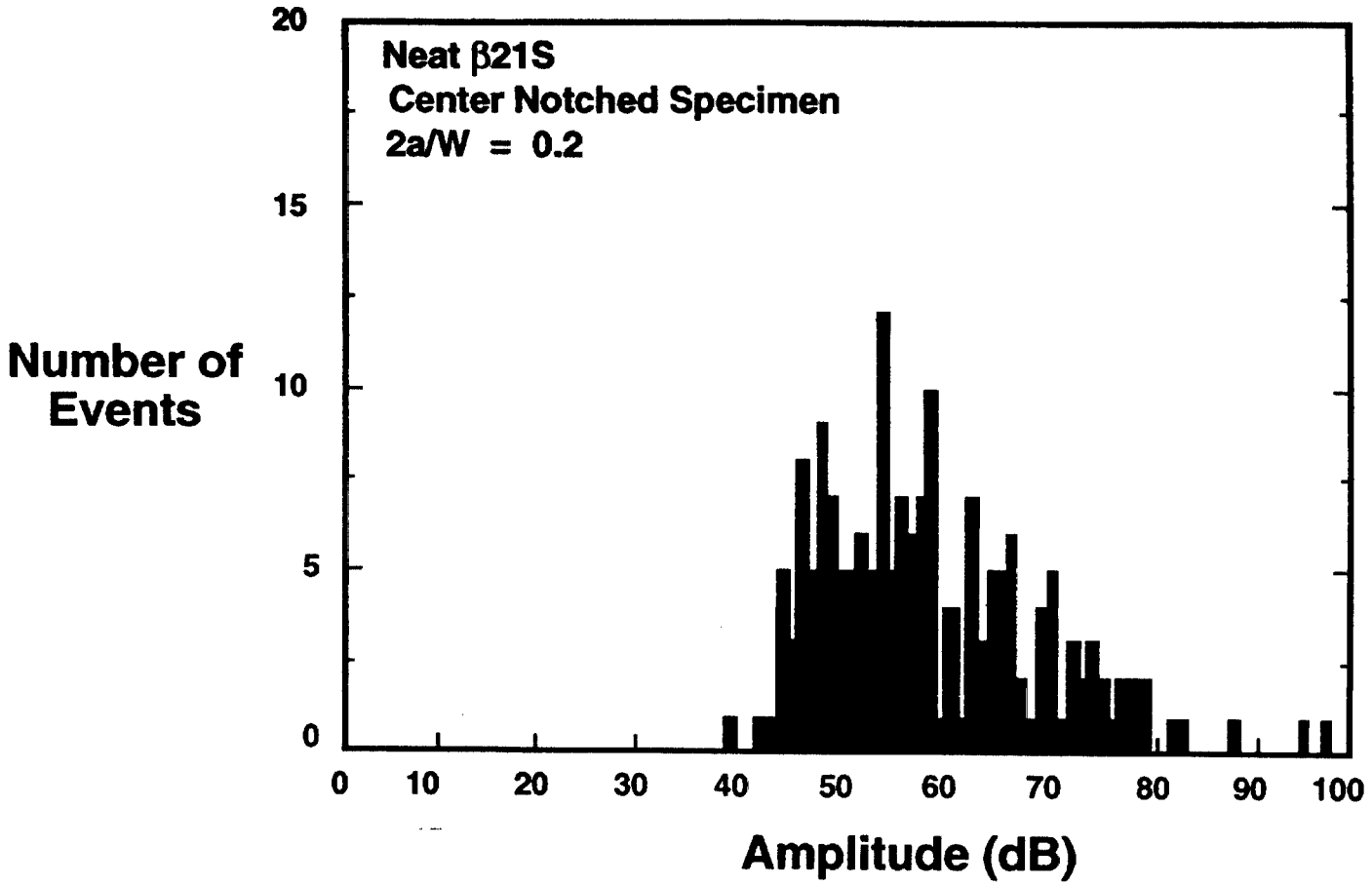

Figure 16. Amplitude distribution histogram of events generated between two sensors on a center notched neat β21S specimen during static loading.

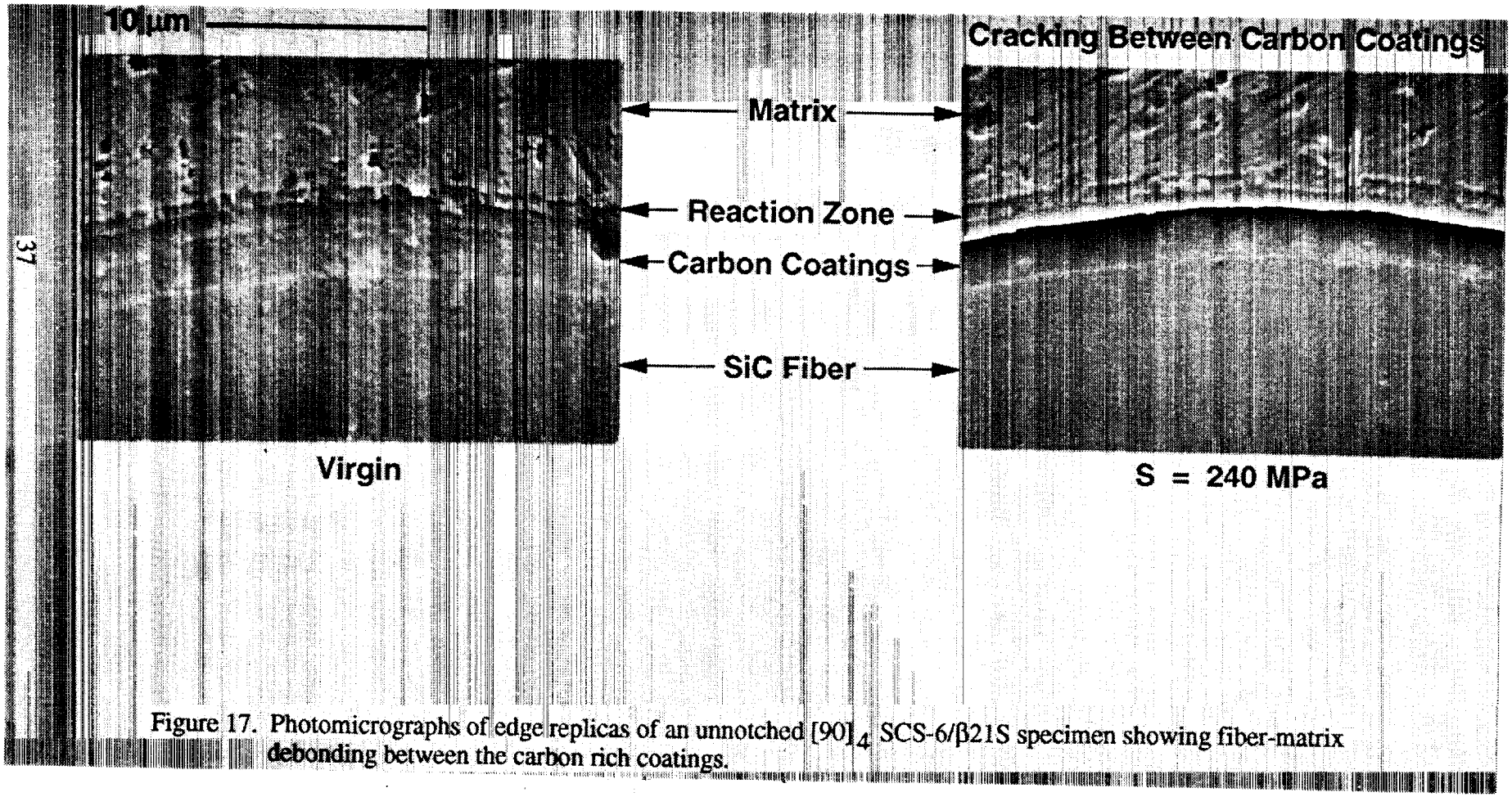

Figure 17. Photomicrographs of edge replicas of an unnotched $[90]_4$ SCS-6/β21S specimen showing fiber-matrix debonding between the carbon rich coatings.

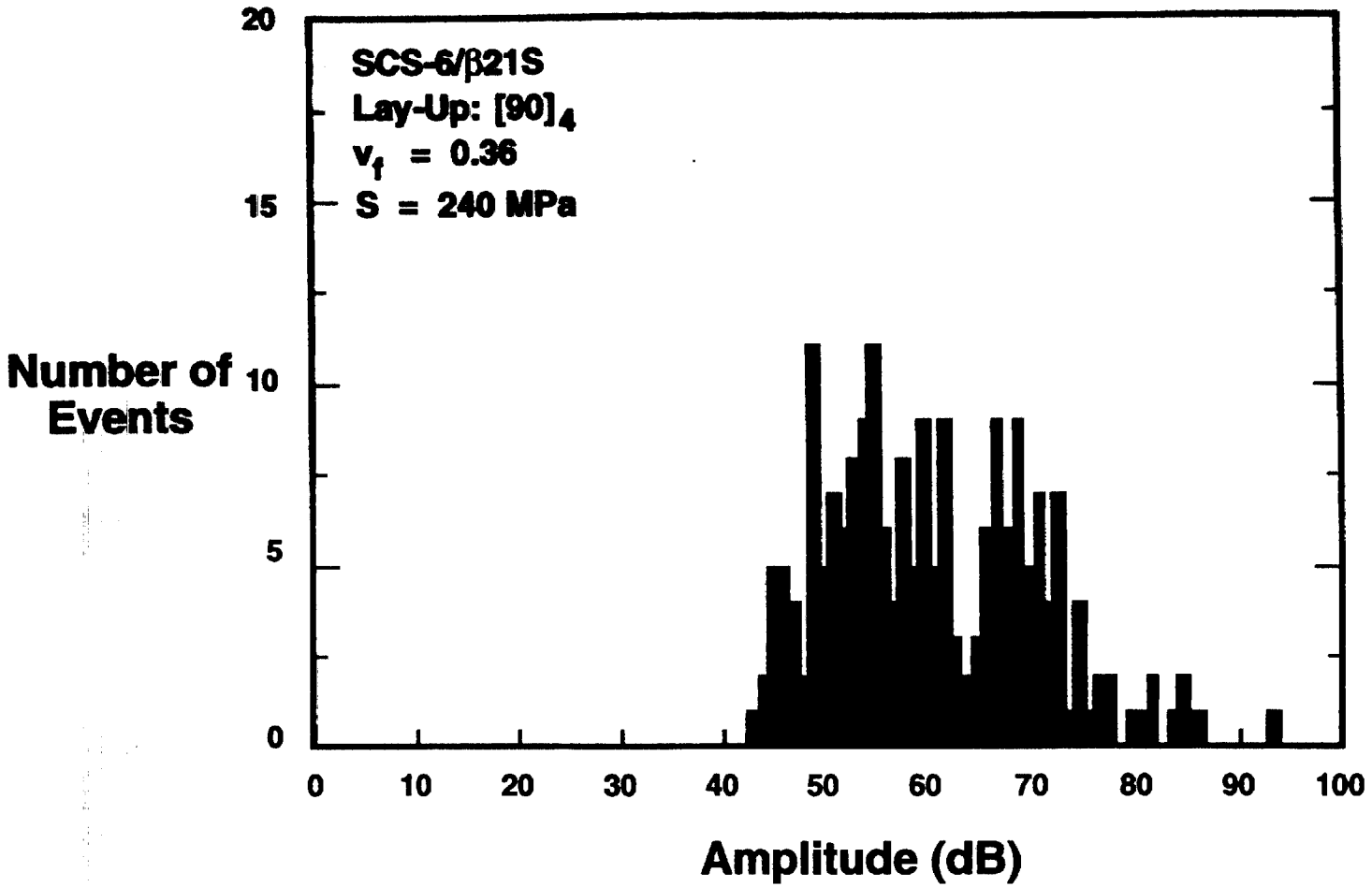

Figure 18. Amplitude distribution histogram of events generated between two sensors on an unnotched $[90]_4$ SCS-6/β21S specimen during static loading.

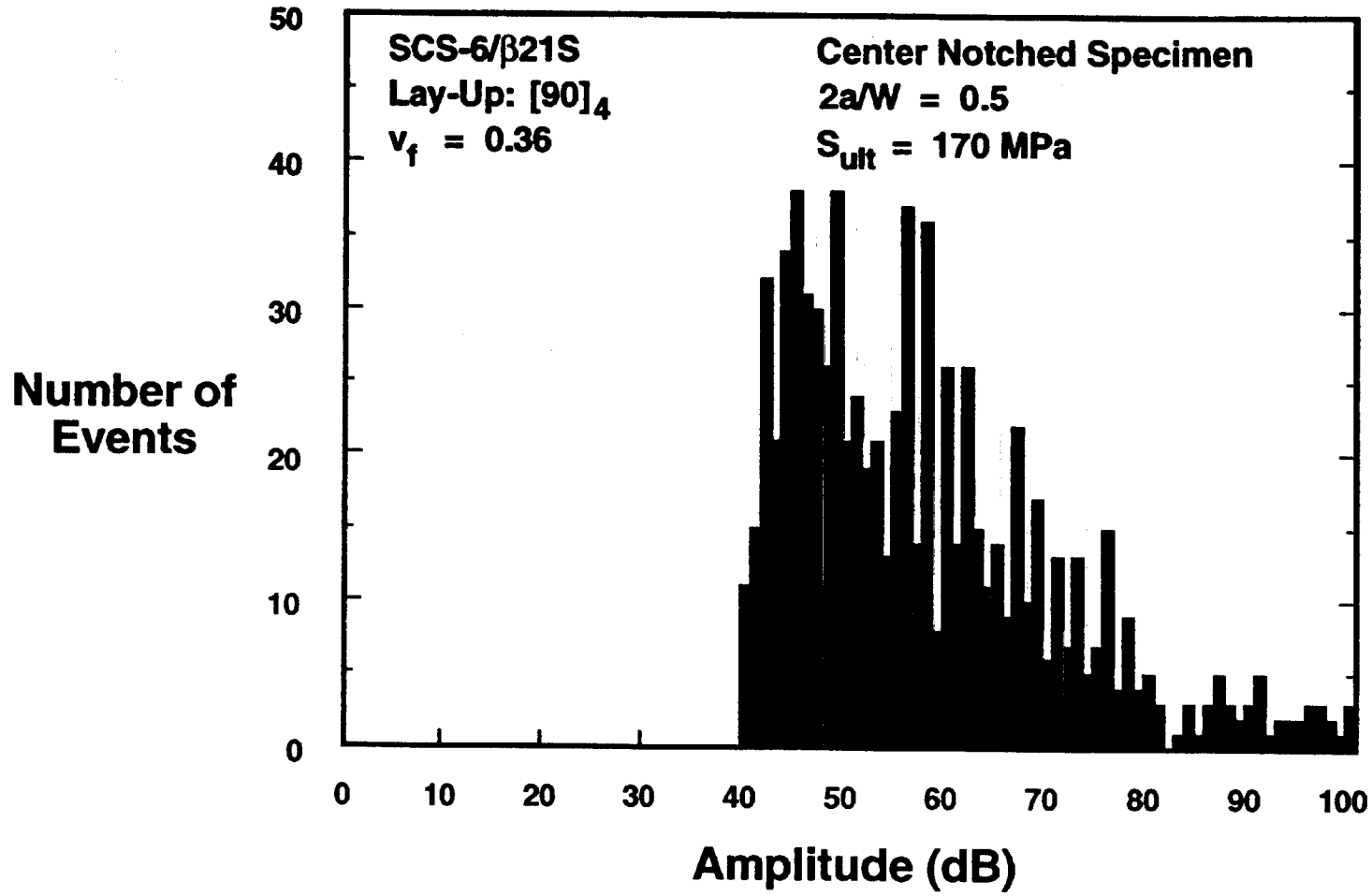

Figure 19. Amplitude distribution histogram of events generated between two sensors on a center notched $[90]_4$ SCS-6/β21S specimen during static loading.

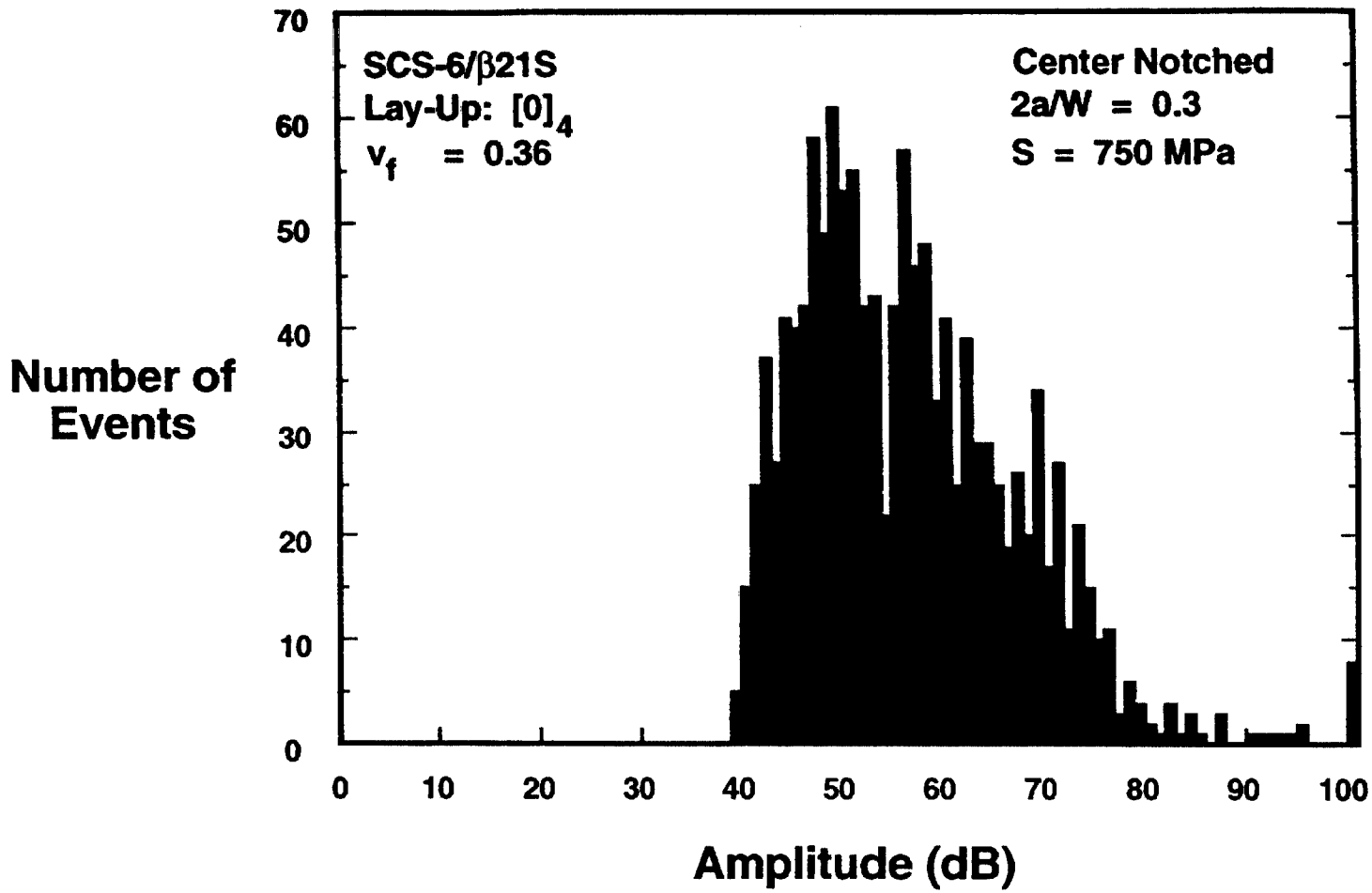

Figure 20. Amplitude distribution histogram of events generated between two sensors on a center notched $[0]_4$ SCS-6/β21S specimen during static loading.

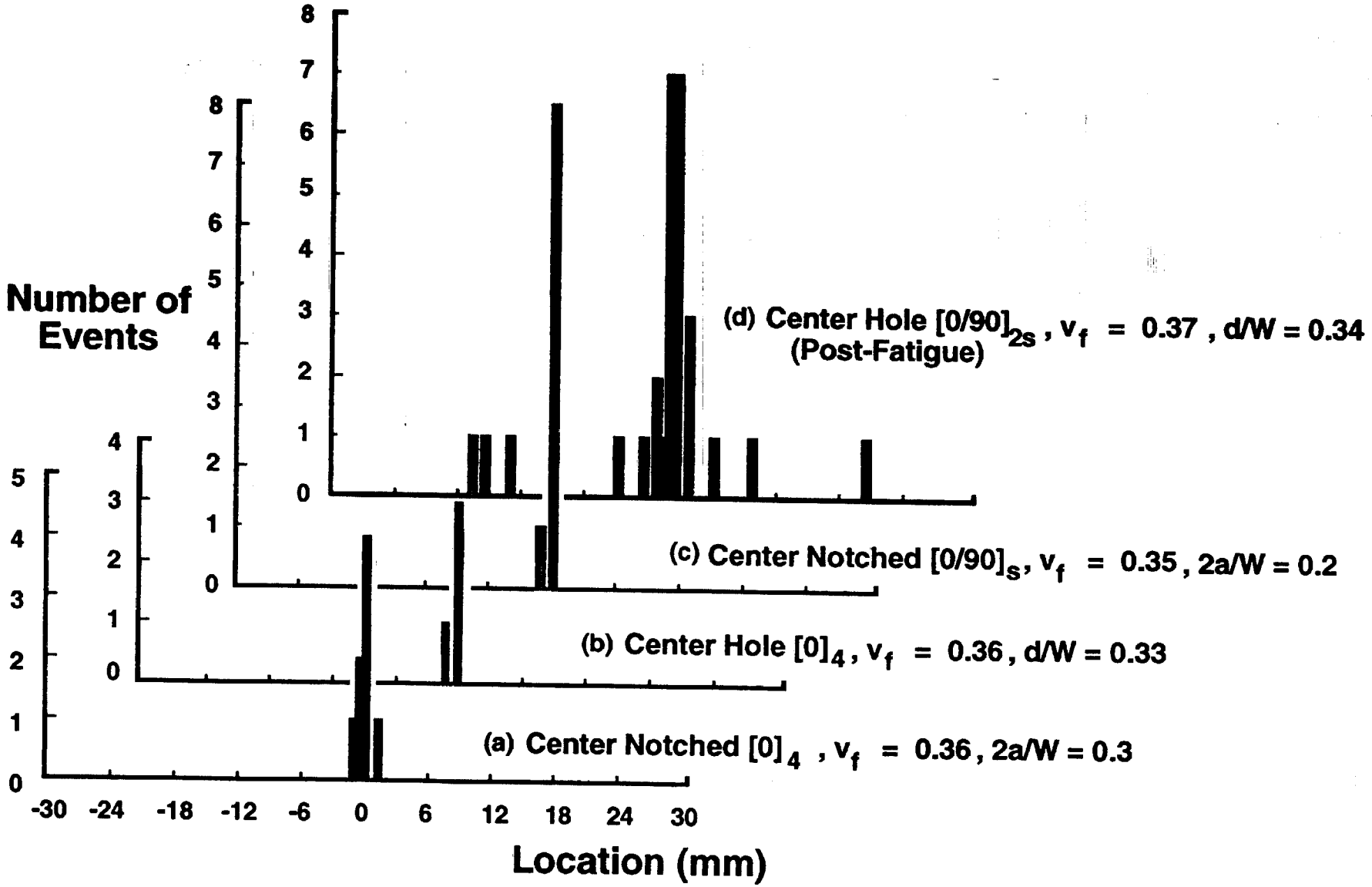

Figure 21. Location distribution histogram of events greater than 99dB generated between two sensors on several notched SCS-6/β21S specimens during static loading: (a) center notched $[0]_4$; (b) center hole, $[0]_4$; (c) center notched $[0/90]_S$; (d) center hole, $[0/90]_{2S}$ subjected to prior fatigue loading, S_{max}= 150 MPa, R = 0.1, frequency = 10 Hz, N = 300,000 cycles.

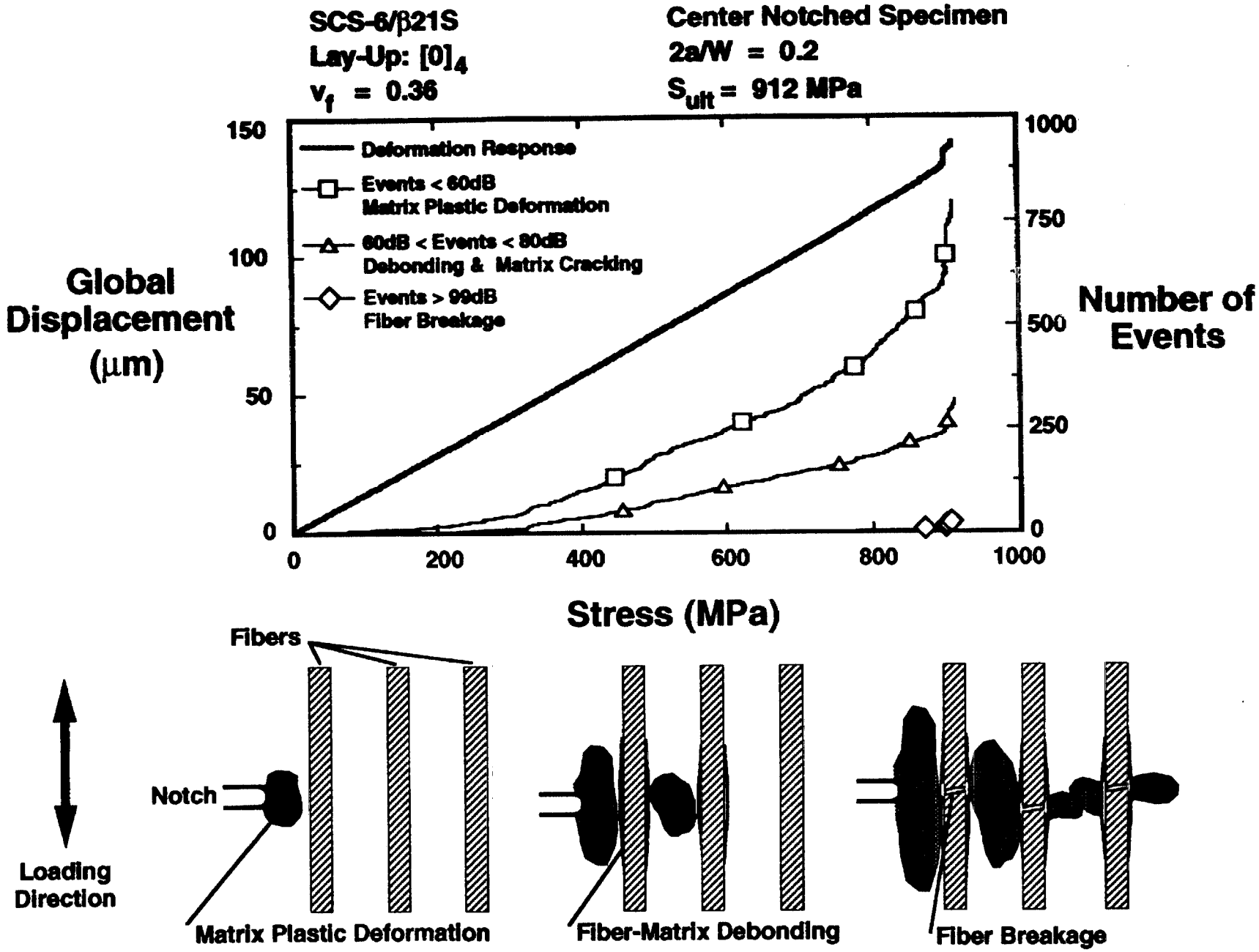

Figure 22. Monitoring damage growth in $[0]_4$ SCS-6/β21S specimen using AE event amplitude.

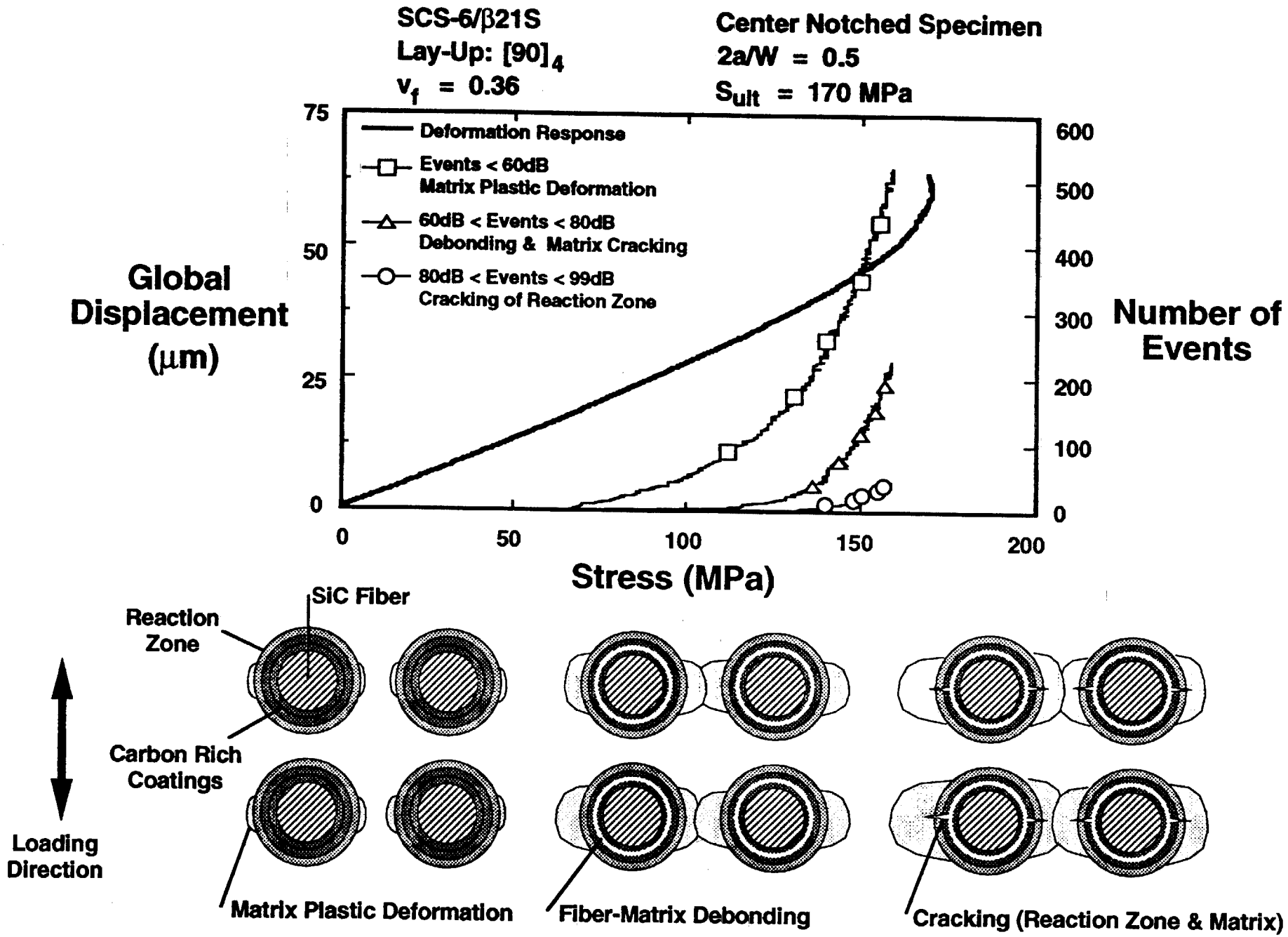

Figure 23. Monitoring damage growth in $[90]_4$ SCS-6/β21S specimen using AE event amplitude.

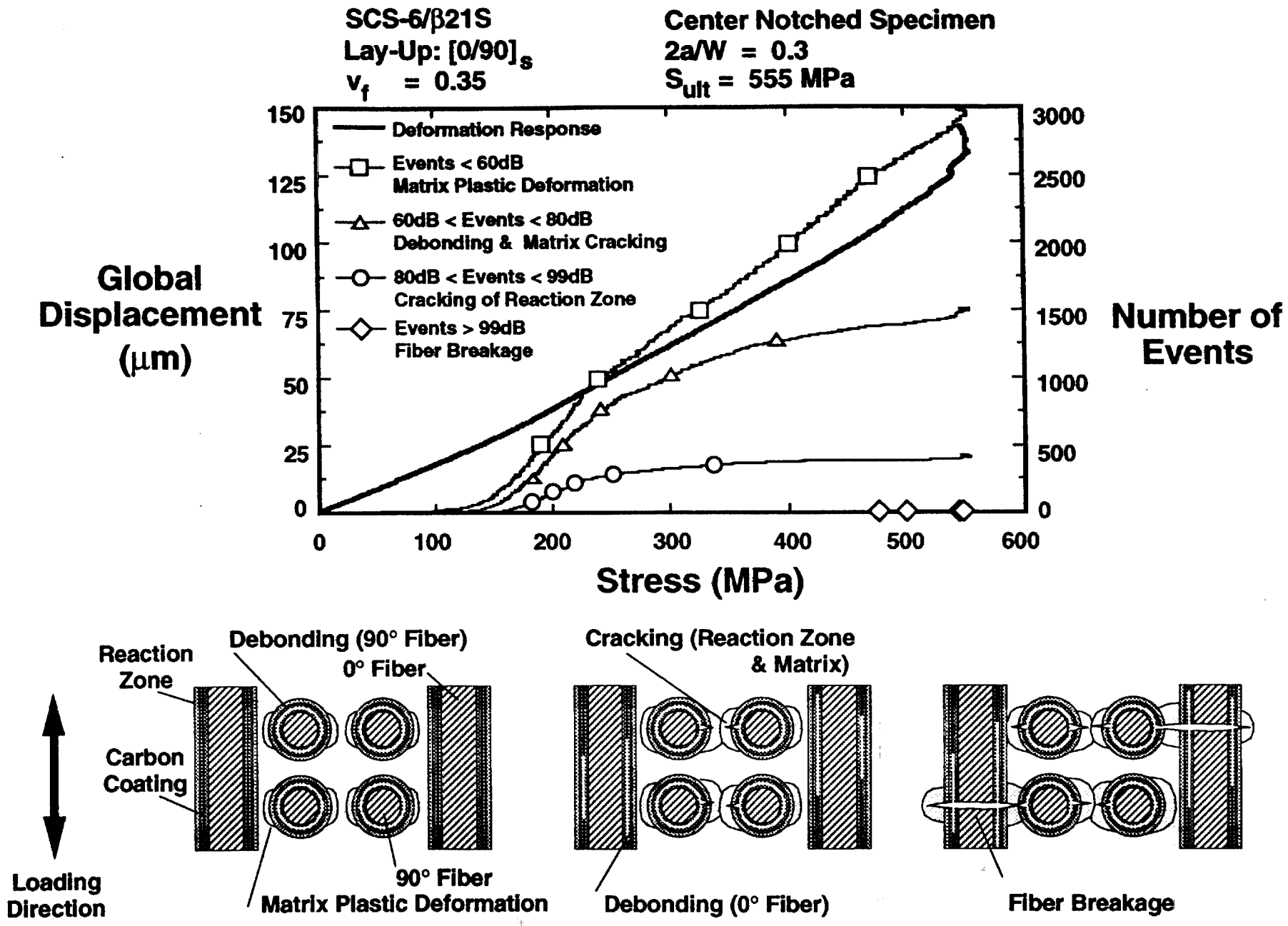

Figure 24. Monitoring damage growth in $[0/90]_s$ SCS-6/β21S specimen using AE event amplitude.

REPORT DOCUMENTATION PAGE

Form Approved
OMB No. 0704-0188

1. AGENCY USE ONLY (Leave blank)	2. REPORT DATE	3. REPORT TYPE AND DATES COVERED
	March 1993	Technical Memorandum

4. TITLE AND SUBTITLE
Monitoring Damage Growth in Titanium Matrix Composites Using Acoustic Emission

5. FUNDING NUMBERS
WU 763-23-45-85

6. AUTHOR(S)
J.G. Bakuckas, Jr.; W.H. Prosser; and W.S. Johnson

7. PERFORMING ORGANIZATION NAME(S) AND ADDRESS(ES)
NASA Langley Research Center
Hampton, VA 23681

8. PERFORMING ORGANIZATION REPORT NUMBER

9. SPONSORING / MONITORING AGENCY NAME(S) AND ADDRESS(ES)
National Aeronautics and Space Administration
Washington, DC 20546-0001

10. SPONSORING / MONITORING AGENCY REPORT NUMBER
NASA TM-107742

11. SUPPLEMENTARY NOTES
Bakuckas: National Research Council Resident Research Asssociate, NASA Langey Research Center, Hampton, VA; Prosser: Research Scientist, NASA Langley Research Center, Hampton, VA; Johnson: Senior Reserch Scientist, Langley.

12a. DISTRIBUTION / AVAILABILITY STATEMENT
Unclassified - Unlimited

Subject Category 24

12b. DISTRIBUTION CODE

13. ABSTRACT *(Maximum 200 words)*

In this study, the application of the acoustic emission (AE) technique to locate and monitor damage growth in titanium matrix composites (TMC) was investigated. Damage growth was studied using several optical techniques including a long focal length, high magnification microscope system with image acquisition capabilities. Fracture surface examinations were conducted using a scanning electron microscope (SEM). The AE technique was used to locate damage based on the arrival times of AE events between two sensors. Using model specimens exhibiting a dominant failure mechanism, correlations were established between the observed damage growth mechanisms and the AE results in terms of the events amplitude. These correlations were used to monitor the damage growth process in laminates exhibiting multiple modes of damage. Results from this study revealed that the AE technique is a viable and effective tool to monitor damage growth in TMC.

14. SUBJECT TERMS
Failure mechanisms; Nondestructive evaluation(NDE); Fiber breakage; Fiber-matrix debonding; Matrix cracking; Matrix plastic deformation; Damage locations

15. NUMBER OF PAGES
45

16. PRICE CODE
A03

17. SECURITY CLASSIFICATION OF REPORT	18. SECURITY CLASSIFICATION OF THIS PAGE	19. SECURITY CLASSIFICATION OF ABSTRACT	20. LIMITATION OF ABSTRACT
Unclassified	Unclassified		